JOURNAL OF GEOPHYSICAL RESEARCH, VOL. 115, E00D18, doi:10.1029/2009JE003354, 2010

Spectral and stratigraphic mapping of hydrated sulfate and phyllosilicate-bearing deposits in northern Sinus Meridiani, Mars

Sandra M. Wiseman,[1] R. E. Arvidson,[1] R. V. Morris,[2] F. Poulet,[3] J. C. Andrews-Hanna,[4] J. L. Bishop,[5,6] S. L. Murchie,[7] F. P. Seelos,[7] D. Des Marais,[6] and J. L. Griffes[8]

Received 2 February 2009; revised 23 September 2009; accepted 22 December 2009; published 2 July 2010.

[1] We present detailed stratigraphic and spectral analyses that focus on a region in northern Sinus Meridiani located between 1°N to 5°N latitude and 3°W to 1°E longitude. Several stratigraphically distinct units are defined and mapped using morphologic expression, spectral properties, and superposition relationships. Previously unreported exposures of hydrated sulfates and Fe/Mg smectites are identified using MRO CRISM and MEX OMEGA near-infrared (1.0 to 2.5 μm) spectral reflectance observations. Layered deposits with monohydrated and polyhydrated sulfate spectral signatures that occur in association with a northeast-southwest trending valley are reexamined using high-resolution CRISM, HiRISE, and CTX images. Layers that are spectrally dominated by monohydrated and polyhydrated sulfates are intercalated. The observed compositional layering implies that multiple wetting events, brine recharge, or fluctuations in evaporation rate occurred. We infer that these hydrated sulfate-bearing layers were unconformably deposited following the extensive erosion of preexisting layered sedimentary rocks and may postdate the formation of the sulfate- and hematite-bearing unit analyzed by the MER Opportunity rover. Therefore, at least two episodes of deposition separated by an unconformity occurred. Fe/Mg phyllosilicates are detected in units that predate the sulfate- and hematite-bearing unit. The presence of Fe/Mg smectite in older units indicates that the relatively low pH formation conditions inferred for the younger sulfate- and hematite-bearing unit are not representative of the aqueous geochemical environment that prevailed during the formation and alteration of earlier materials. Sedimentary deposits indicative of a complex aqueous history that evolved over time are preserved in Sinus Meridiani, Mars.

Citation: Wiseman, S. M., R. E. Arvidson, R. V. Morris, F. Poulet, J. C. Andrews-Hanna, J. L. Bishop, S. L. Murchie, F. P. Seelos, D. Des Marais, and J. L. Griffes (2010), Spectral and stratigraphic mapping of hydrated sulfate and phyllosilicate-bearing deposits in northern Sinus Meridiani, Mars, *J. Geophys. Res.*, *115*, E00D18, doi:10.1029/2009JE003354.

1. Introduction

[2] Geomorphic and/or spectral evidence for past aqueous activity is preserved in multiple units that occur within Sinus Meridiani, Mars. Fluvially dissected Noachian-aged cratered terrain is unconformably overlain by extensive outcrops of hydrous light-toned sedimentary rock [*Malin and Edgett*, 2000; *Edgett and Malin*, 2002; *Hynek et al.*, 2002; *Arvidson et al.*, 2003; *Gendrin et al.*, 2005; *Poulet et al.*, 2008]. The Meridiani Planum sulfate and hematite-bearing unit investigated by the Mars Exploration Rover (MER) Opportunity [*Squyres et al.*, 2004a] occurs near the top of the stratigraphic section exposed in Sinus Meridiani [*Christensen et al.*, 2001b; *Hynek et al.*, 2002; *Arvidson et al.*, 2003; *Christensen and Ruff*, 2004].

[3] In this paper we present detailed stratigraphic and spectral analyses that focus on a region in northern Sinus Meridiani located between 1°N to 5°N latitude and 3°W to 1°E longitude. The presence of outcrops with well exposed contacts and distinctive spectral signatures facilitates stratigraphic analyses in this region. Several stratigraphically distinct units were defined and mapped within the study area based on morphologic expression and superposition

[1]McDonnell Center for the Space Sciences, Department of Earth and Planetary Sciences, Washington University in Saint Louis, Saint Louis, Missouri, USA.
[2]NASA Johnson Space Center, Houston, Texas, USA.
[3]Institut d' Astrophysique Spatiale, Université Paris-Sud, Orsay, France.
[4]Department of Geophysics, Colorado School of Mines, Golden, Colorado, USA.
[5]SETI Institute, Mountain View, California, USA.
[6]NASA Ames Research Center, Moffett Field, California, USA.
[7]Johns Hopkins University Applied Physics Laboratory, Laurel, Maryland, USA.
[8]Division of Geological and Planetary Sciences, California Institute of Technology, Pasadena, California, USA.

0148-0227/10/2009JE003354

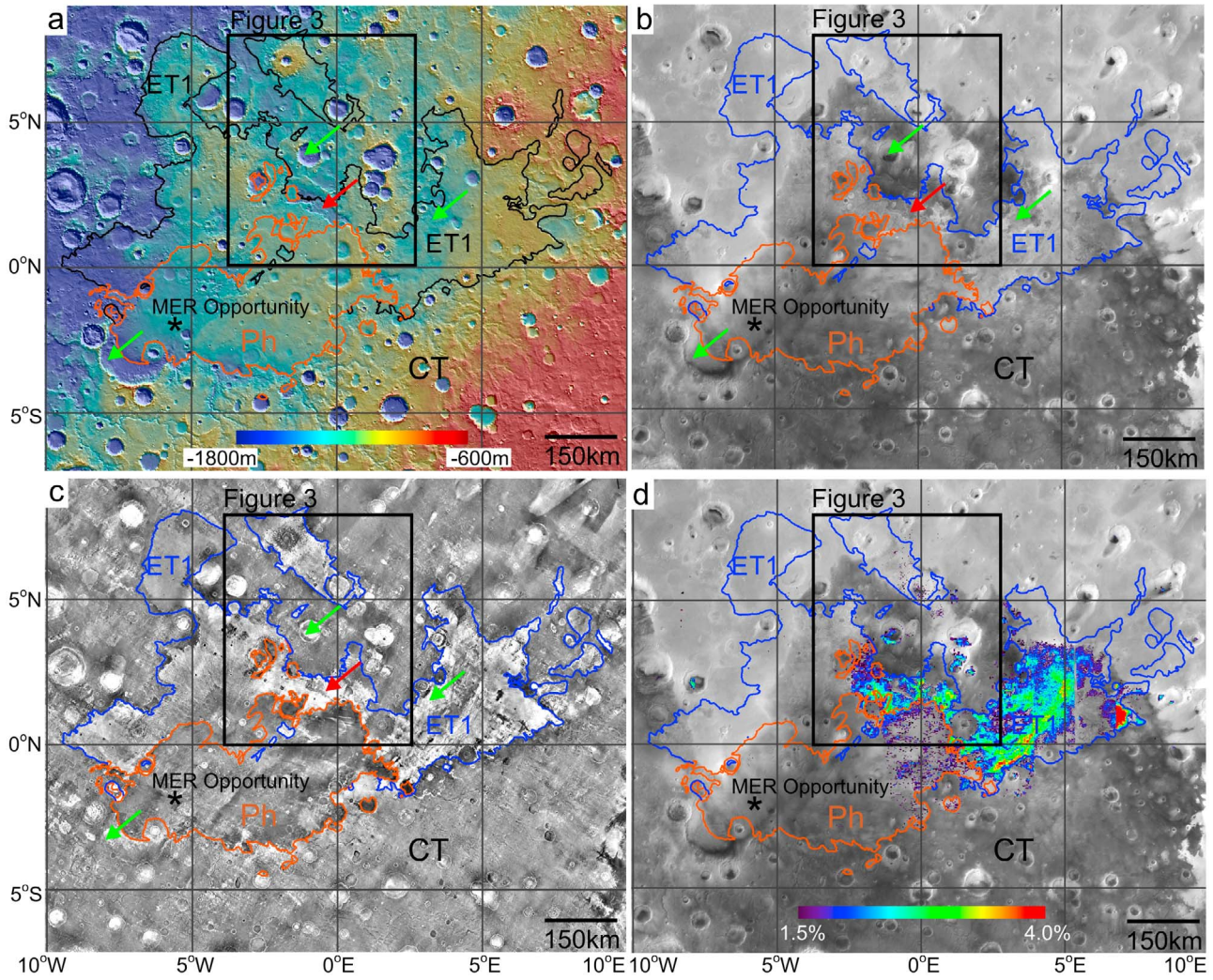

Figure 1. Regional context maps showing main units (Table 1) exposed in Sinus Meridiani. Cratered Terrain (CT) is unconformably overlain by indurated sedimentary rock, Etched Terrain 1 (ET1). The Plains, Hematite-bearing (Ph) is the stratigraphically youngest mapped unit and consists of indurated sedimentary rock, Etched Terrain 2 (ET2), overlain by an unconsolidated veneer, the Plains Mantle, Hematite-bearing (Pm). Locations of previously identified Fe/Mg phyllosilicates [*Poulet et al.*, 2005, 2008; *Wiseman et al.*, 2008] and hydrated sulfates [*Gendrin et al.*, 2005; *Griffes et al.*, 2007] are indicated with green and red arrows, respectively. Detailed mapping presented in Figure 4 indicates that deposits in the valley indicated with a red arrow are stratigraphically distinct from ET1. Early Hesperian volcanic ridged plains cover a small portion of CT in western Sinus Meridiani near 1°S, 9°W [*Scott and Tanaka*, 1986]. Some intracrater deposits within craters in CT may be relatively younger than CT and are not distinguished in this map. (a) MOLA shaded relief map overlain by color-coded topography. (b) MOC WA mosaic. (c) THEMIS NIR mosaic. (d) OMEGA D1900 (Table 2) parameter map, which indicates the presence of hydrated phases, overlain on a MOC WA mosaic.

relationships. Previously identified layered deposits with monohydrated and polyhydrated sulfate spectral signatures [*Arvidson et al.*, 2005; *Gendrin et al.*, 2005; *Griffes et al.*, 2007] are reexamined using higher-resolution Mars Reconnaissance Orbiter (MRO) Compact Reconnaissance Imaging Spectrometer for Mars (CRISM) [*Murchie et al.*, 2007], Context Imager (CTX) [*Malin et al.*, 2007], and High Resolution Imaging Science Experiment (HiRISE) [*McEwen et al.*, 2007] data. Additional hydrated sulfate and Fe/Mg phyllosilicate-bearing exposures are identified using MRO CRISM and Mars Express (MEX) Observatoire pour la Minéralogie, l'Eau, les Glaces et l'Activité (OMEGA) [*Bibring et al.*, 2004] near-infrared (NIR) (1.0 to 2.5 μm) spectral reflectance observations.

2. Geologic Context

[4] The Sinus Meridiani region of Mars, formerly termed Terra Meridiani, is located near the southwestern margin of Arabia Terra and is centered at 5°S, 0°E. Heavily cratered Noachian-aged terrain that has an ancient regional slope to the northwest [*Phillips et al.*, 2001; *Andrews-Hanna et al.*,

Table 1. Unit Descriptions[a]

Unit	Unit Description	Subunit	Subunit Description
CT (Cratered Terrain)	Noachian aged, heavily cratered terrain, fluvially dissected, low albedos (0.10 to 0.15), intermediate thermal inertias (200 to 300 tiu). Basaltic spectral signature typical, Fe/Mg smectites detected in some locations.[b]		
ET1 (Etched Terrain 1)	Indurated, exhibits layering at multiple scales and erosional mesas, intermediate albedos (0.17 to 0.22), high thermal intertias (350 to 500 tiu). Hydrous spectral signature typical, hydrated sulfates and Fe/Mg smectites detected in some locations.[b]	$ET1_A$	Variable thickness (up to 150 m), small-scale scalloped morphology, brighter than $ET1_B$ and $ET1_C$. Spectrally bland.[b]
		$ET1_B$	40–50 m thick, relatively smooth. Weak hydrated spectral signature typical.[b]
		$ET1_C$	10–30 m thick, erosional knobs and ridges. Hydrous, Fe/Mg smectites detected.[b]
		$ET1_D$	70 m thick, multiple layers. Strong hydrated spectral signature.[b]
Ph (Plains, Hematite-bearing)	Composite unit consisting of an indurated unit, Etched Terrain 2 (ET2), overlain by an unconsolidated veneer, Plains Mantle, Hematite-bearing (Pm). Location of the MER Opportunity rover landing site is shown in Figure 1. Low albedos (0.12 to 0.16), intermediate thermal inertias (150 to 250 tiu). Spectrally bland.[b]	ET2	Indurated, variable thickness (up to 300 m in study area), sulfate-rich (based on MER Opportunity rover observations), contains hematitic concretions.
		Pm	Unconsolidated veneer (0 to 1 m thick near Opportunity site), mainly composed of unaltered to weakly altered basaltic sand. Contains a lag of hematitic concretions derived from erosion of ET2.
		LHS[c]	Indurated, exhibits layering, mesas, pits, and grooves. Spectrally dominated by monohydrated and polyhydrated sulfates.[b]
		LHS_{cap}[c]	Indurated, brighter than LHS, relatively smooth. Strong hydrated spectral signature.[b]

[a]Units are listed in stratigraphic order from older to youngest. TES bolometric albedo [*Christensen et al.*, 2001a] and TES thermal inertia values [*Mellon et al.*, 2000] were derived from products available through the Planetary Data System that were binned at 8 pixels/degree.

[b]Based on OMEGA and CRISM spectral analyses (1.0 to 2.5 μm).

[c]LHS and LHS_{cap} were included as part of ET1 in the regional context map (Figure 1), but more detailed mapping in the study area (Figure 4b) revealed that LHS and LHS_{cap} are stratigraphically distinct from ET1. LHS and LHS_{cap} may postdate ET2 formation (section 5.2).

2008] is exposed at the base of the stratigraphic section in Sinus Meridiani. The Noachian cratered terrain was fluvially dissected and unconformably overlain by light-toned indurated sedimentary rock referred to as "etched" terrain [*Hynek et al.*, 2002; *Arvidson et al.*, 2003]. Low-albedo, hematite-bearing plains overlie the etched unit and dominate the surface of central Sinus Meridiani, Meridiani Planum [*Christensen et al.*, 2001b; *Hynek et al.*, 2002; *Arvidson et al.*, 2003].

[5] To facilitate discussion of our study area, we present an updated regional context map of Sinus Meridiani that is broadly similar to previous maps (Figure 1) [e.g., *Hynek et al.*, 2002; *Arvidson et al.*, 2003; *Hynek*, 2004]. Materials are subdivided into Cratered Terrain (CT), Etched Terrain 1 (ET1), and the Plains, Hematite-bearing (Ph). ET1 is equivalent to the etched terrain unit mapped by *Hynek et al.* [2002], *Arvidson et al.* [2003], and *Hynek* [2004]. Ph consists of rock overlain by an unconsolidated veneer [e.g., *Arvidson et al.*, 2006]. In this paper, we classified the rock component of Ph as Etched Terrain 2 (ET2) and the unconsolidated veneer as Plains Mantle, Hematite-bearing (Pm). Unit boundaries were mapped using a combination of attributes including morphologic characteristics, topographic expressions, relative thermal properties, selected spectral characteristics, and superposition relationships. Units are described in sections 2.1 through 2.3 (summary provided in Table 1) and a brief overview of postulated formation mechanisms for ET1 and ET2 is presented in section 2.4.

2.1. Cratered Terrain Unit

[6] Although Noachian-aged Cratered Terrain (CT) was subdivided into multiple units in previous work [e.g., *Scott and Tanaka*, 1986; *Hynek et al.*, 2002], this level of distinction is not made in our regional context map (Figure 1). Some of the Noachian-aged craters in CT have prominent yet degraded rims [*Hynek et al.*, 2002] whereas others are almost completely buried or exhibit a flat floored morphology that may have resulted from fluvial erosion and deposition [*Craddock and Howard*, 2002]. CT in southern Sinus Meridiani is heavily dissected by channels that are orientated in the direction of regional slope, to the northwest

(Figure 1a) [*Scott and Tanaka*, 1986; *Hynek et al.*, 2002]. A relatively intense episode of fluvial erosion occurred during the late Noachian period that reactivated preexisting channels and carved additional fluvial features in southern Sinus Meridiani [*Hynek and Phillips*, 2001, 2008].

[7] Areas mapped as CT that appear bright in Figure 1b are mantled by aeolian dust deposits [*Arvidson et al.*, 2003]. CT surfaces that are not mantled by dust generally have low albedos [*Arvidson et al.*, 2003], intermediate thermal inertias [*Hynek et al.*, 2002; *Arvidson et al.*, 2003], and a basaltic spectral signature [*Poulet et al.*, 2008] (Table 1). Higher thermal inertia materials are exposed in some intracrater deposits and on limited intercrater surfaces. In addition, Fe/Mg phyllosilicate-bearing materials were previously identified in limited locations within CT (Figure 1, green arrows) [*Poulet et al.*, 2008; *Wiseman et al.*, 2008].

2.2. Etched Terrain 1 Unit

[8] The Etched Terrain 1 (ET1) unit unconformably overlies CT and is composed of relatively high thermal inertia indurated material [*Mellon et al.*, 2000; *Malin and Edgett*, 2000; *Edgett and Malin*, 2002; *Hynek et al.*, 2002; *Arvidson et al.*, 2003; *Putzig and Mellon*, 2007] that is at least 300 m thick in some areas. ET1 is laterally extensive across Sinus Meridiani and is characterized by intermediate albedos and relatively high thermal inertias (Table 1) [*Arvidson et al.*, 2003; *Hynek*, 2004]. Surfaces of ET1 are subhorizontal and typically dip between ~0.05° to 1.0° in the direction of regional slope, to the northwest [*Hynek and Phillips*, 2008]. ET1 exhibits layering at multiple scales [*Malin and Edgett*, 2000; *Edgett*, 2005] and the presence of erosional mesas and grooves indicates variable material properties among layers [*Arvidson et al.*, 2003; *Edgett*, 2005]. ET1 consists of several stratigraphically distinct subunits that are not distinguished in this regional context map, but are detailed in section 4.

[9] ET1 is inferred to have formed during the late Noachian to early Hesperian period [*Hynek et al.*, 2002]. Along its southern margin, ET1 embays several channel features that were incised into CT. However, there is some evidence that channel features that formed during the late Noachian also cut lower layers of ET1 [*Hynek and Phillips*, 2008].

[10] Although the western margin of ET1 is mantled with bright dust (Figure 1b), this area is mapped as ET1 because it is laterally continuous with and morphologically similar to unmantled areas. The central and eastern portions of ET1 are well exposed and have higher thermal inertias than other portions of the unit (Figure 1c) [e.g., *Hynek*, 2004]. Hydrous materials were detected in OMEGA spectral reflectance observations more frequently in areas of ET1 with the highest thermal inertias (Figure 1d) [*Poulet et al.*, 2008]. Previously identified areas of ET1 that exhibit distinctive hydrated sulfate or Fe/Mg phyllosilicate spectral signatures are indicated in Figure 1 (red and green arrows, respectively) [*Gendrin et al.*, 2005; *Griffes et al.*, 2007; *Poulet et al.*, 2008].

2.3. Plains, Hematite-Bearing Unit

[11] The Plains, Hematite-bearing (Ph) unit is a composite unit that consists of rock, Etched Terrain 2 (ET2), overlain by an unconsolidated veneer, the Plains Mantle, Hematite-bearing (Pm). ET2 occurs stratigraphically above ET1 [*Hynek et al.*, 2002; *Arvidson et al.*, 2003]. The surface of Ph is aerially dominated by Pm, although patches of ET2 are visible in some locations in high-resolution orbital images of Ph. Gray crystalline hematite was detected at the surface of Ph in Mars Global Surveyor (MGS) Thermal Emission Spectrometer (TES) [*Christensen et al.*, 2001a] infrared (IR) spectra [*Christensen et al.*, 2000a, 2001b].

[12] In situ investigations of Ph made by the MER Opportunity rover (landing site indicated in Figure 1) revealed that the bedrock component of Ph (ET2) in the vicinity of the landing site is composed of ~20 wt % SO_3, contains jarosite at the ~10 wt % level [*Klingelhöfer et al.*, 2004; *Morris et al.*, 2006], and contains hematitic concretions. Positive correlations between Mg and S in Alpha Particle X-Ray Spectrometer data suggest the presence of Mg-bearing sulfate minerals in ET2 [*Rieder et al.*, 2004; *Clark et al.*, 2005]. The bulk of Pm is composed of low-albedo basaltic sand [*Christensen et al.*, 2000b] that was transported into the region via aeolian processes and was not derived from erosion of the underlying friable sulfate-rich rock [*Squyres et al.*, 2004a; *Arvidson et al.*, 2006]. The hematite signature detected in orbital TES IR spectra of Ph results from hematitic concretions that weathered out from ET2 and were concentrated as a surface lag via aeolian processes [*Squyres et al.*, 2004a; *Morris et al.*, 2006; *Arvidson et al.*, 2006].

[13] Ph is a few hundred meters thick in some areas but is an order of magnitude thinner near its northern margin. Crater counting of Ph indicates a late Noachian to early Hesperian age for ET2 [*Arvidson et al.*, 2006] whereas crater counting restricted to small craters (<250 m diameter) suggests a late Amazonian crater retention age for Pm [*Lane et al.*, 2003]. *Christensen and Ruff* [2004] noted that the extent of the hematite-bearing mantle is largely controlled by the extent of underlying bedrock. Because the bedrock component (ET2) and the mantle component (Pm) of Ph appear to be coupled, the extent of Pm is a proxy for the presence of underlying ET2. TES hematite index values area variable across the unit mapped as Ph in this paper and mesas with low hematite index values that may represent remnants of a hematite-free unit above Ph [*Christensen and Ruff*, 2004] were not distinguished.

[14] OMEGA spectra of Ph are relatively flat between 1.0 to 2.5 μm and are consistent with a mixture of unaltered to weakly altered basaltic sand, gray hematite, and nanophase iron oxides [*Arvidson et al.*, 2006]. Distinctive H_2O and/or OH related spectral absorption features indicative of hydrated and/or hydroxylated sulfates were not identified in OMEGA spectra of Ph. Initial analyses of higher-resolution CRISM spectra over the Opportunity rover landing site [*Wiseman et al.*, 2007] are consistent with *Arvidson et al.* [2006].

2.4. Formation Mechanisms for ET1 and ET2

[15] A brief discussion of proposed formation mechanisms for ET2 is presented first because more observational constraints exist for it than for ET1. The bedrock explored by the Opportunity rover, part of ET2, is most commonly interpreted as a "dirty" sulfate-rich evaporitic deposit composed of reworked materials that formed in an interdune playa environment [e.g., *Squyres et al.*, 2004b; *Grotzinger et al.*, 2005; *Arvidson et al.*, 2006; *McLennan et al.*, 2005; *Morris et al.*, 2006; *Squyres et al.*, 2006]. Other formation hypotheses including volcanic [*McCollom and Hynek*,

2005], impact surge [*Knauth et al.*, 2005], and ice weathering [*Niles and Michalski*, 2009] were also proposed. Although most outcrops investigated by the Opportunity rover are interpreted as cemented aeolian deposits, some primary sedimentary features consistent with subaqueous deposition are also observed [*Grotzinger et al.*, 2005]. The hematitic concretions within ET2 could have formed via hydrolysis of jarosite during diagenesis [*McLennan et al.*, 2005; *Golden et al.*, 2008]. The presence of jarosite implies that low pH (1–4) [*Stoffregen et al.*, 2000; *Morris et al.*, 2006] and oxidizing aqueous conditions occurred during formation and/or diagenesis of ET2.

[16] Regardless of the sediment source, ET2 experienced aqueous alteration, likely within a groundwater-dominated environment [*Squyres et al.*, 2006; *Arvidson et al.*, 2006; *Andrews-Hanna et al.*, 2007, 2010]. A hydrologic model that includes rainfall, groundwater infiltration, and groundwater emergence predicts that some sites in Sinus Meridiani hosted persistent groundwater emergence and evaporation driven by the unique topography of the southwestern Arabia Terra region [*Andrews-Hanna et al.*, 2007, 2010]. Groundwater upwelling in the absence of an enclosing basin provides a plausible mechanism for the extensive formation of evaporitic deposits in Meridiani Planum.

[17] Prior to the MER Opportunity and the MEX OMEGA missions, several authors suggested a sedimentary aeolian or pyroclastic origin for ET1 [e.g., *Schultz and Lutz*, 1988; *Chapman and Tanaka*, 2002; *Hynek et al.*, 2002; *Arvidson et al.*, 2003]. Subaqueous deposition was also considered [*Edgett and Parker*, 1997]. However, after evaporitic process were inferred from Opportunity rover observations of overlying ET2 materials and hydrated exposures were detected in OMEGA spectra of ET1, *Arvidson et al.* [2006] and *Poulet et al.* [2008] favored formation of ET1 in groundwater driven regimes. The differences in spectral and morphologic characteristics between ET1 and ET2 suggest that geochemical conditions differed during the formation of these two units. More neutral or mildly acidic aqueous conditions likely transitioned to the low pH geochemical environment inferred from the presence of jarosite in ET2 [*Poulet et al.*, 2008].

3. Data Sets and Methods

3.1. CRISM and OMEGA Data Preprocessing

[18] The CRISM spectrometer aboard MRO is a hyperspectral imager that has short (S) and long (L) wavelength detectors that operate between 0.36 to 1.06 μm and 1.00 to 3.94 μm, respectively [*Murchie et al.*, 2007, 2009a]. CRISM is capable of acquiring both hyperspectral (544 channels) and multispectral (72 band subset) images. Twenty m/pixel hyperspectral full resolution targeted (FRT) images, 40 m/pixel hyperspectral half resolution long (HRL) and short (HRS) targeted images, 200 m/pixel multispectral survey (MSP) images, and 100 m/pixel multispectral window (MSW) images were analyzed. The CRISM spectrometer utilizes 2-D detector arrays that cause slight column dependencies in CRISM spectral data [*Murchie et al.*, 2007].

[19] The OMEGA spectrometer [*Bibring et al.*, 2004, 2005] covers the wavelength range from 0.35 to 5.1 μm in 352 channels using VNIR (0.35 to 1.07 μm), C (0.93 to 2.70 μm), and L (2.53 to 5.10 μm) detectors. OMEGA images vary in spatial resolution depending on spacecraft altitude and are acquired in 16, 32, 64, or128 pixel modes. Analyses were limited to OMEGA images with spatial resolutions $\leq$ 2.5 km/pixel. The OMEGA spectrometer utilizes a 1-D NIR detector in which images are built up by across track scanning and along-track orbital motion.

[20] Spectral analyses used CRISM L spectrometer and OMEGA C spectrometer data and focused on the NIR wavelength region between 1.0 and 2.5 μm. Hydrated and/or hydroxylated phases exhibit distinctive absorption features in this region of the spectrum, which is dominated by reflected solar radiation and lacks competing effects from thermal emission that occur at longer wavelengths. CRISM and OMEGA I/F spectra (where I is the surface radiance and F is the solar irradiance at the top of the Martian atmosphere) were calibrated as described by *Murchie et al.* [2007, 2009a] and *Bibring et al.* [2004, 2005], respectively. For most analyses, atmospheric gas bands were removed to first order by ratioing I/F spectra to a scaled atmospheric transmission spectrum derived from Olympus Mons high- and low-altitude observations [*Langevin et al.*, 2005; *Mustard et al.*, 2008; *Wiseman*, 2009; S. L. Murchie et al., CRISM Data Product Software Interface Specification, available at http://wwwpds.wustl.edu/missions/mro/index.htm, 2006]. Surface Lambert albedo spectra (i.e., atmospherically corrected spectra assuming isotropic surface scattering) were retrieved from selected CRISM I/F spectra using Discrete Ordinate Radiative Transfer (DISORT) [*Stamnes et al.*, 1988; *Wolff et al.*, 2009] model results. Atmospheric gas and dust contributions were simultaneously accounted for in the DISORT models and removed during atmospheric correction using procedures outlined by *Wiseman* [2009].

[21] Spectral parameter maps designed to detect spectral features at wavelengths of known H_2O and/or OH vibrational features indicative of hydrated and/or hydroxylated phases [e.g., *Pelkey et al.*, 2007] were generated from atmospherically corrected CRISM and OMEGA observations. Parameter calculations and threshold values are defined in Table 2. CRISM parameter maps were spatially filtered to reduce speckling from noise. Isolated pixels with relatively high parameter values were assumed to result from noise and not surface contributions. A sliding kernel was used to determine areas that had a high density of pixels (8 out of 12) with relatively high parameter values (Table 2). All parameter values within the kernel were retained unaltered if the 8 out of 12 criterion was met and parameter values within kernels that did not meet the criterion were set to 0.

[22] Spectral ratios were used to suppress instrumental and/or residual atmospheric artifacts and to highlight spectral features of interest. These ratios were calculated by dividing an atmospherically corrected CRISM spectrum (typically the average of 25 spectra) by a relatively bland spectrum from the same image. Numerator and denominator spectra for spectral ratios were extracted from the same CRISM columns. Because artifacts can be introduced in ratio spectra, the shapes of numerator and denominator spectra were also considered in detailed analyses.

3.2. Identification of Spectral Features

[23] Detailed spectral analyses focused on identification of candidate phases responsible for producing H_2O and/or OH related vibrational features detected in CRISM spectra.

Table 2. Spectral Parameters[a]

Name	Parameter	Formulation	Threshold	Rationale
D1900	1.9 μm band depth	1 − ((R1930)/(0.3*R1830 + 0.7*R2120))	1.5%	H_2O (e.g., trapped H_2O, absorbed H_2O, adsorbed H_2O, or bound H_2O).
D1900FRT	1.9 μm band depth	1 − (((R1930 + R1921 + R1915)/3)/(0.3*R1830 + 0.7*R2120))	Variable	
D2100	2.1 μm band depth	1 − (((R2120 + R2140)*0.5)/(0.62*R1930 + 0.38*R2250))	2%	H_2O (particularly monohydrated sulfate)
D2100FRT	2.1 μm band depth	1 − (((R2120 + R2126 _ R2133 + R2140)*0.25)/(0.62*R1930 + 0.38*R2250))	Variable	
D2300	2.3 μm band depth	1 − ((R2290/CR2290 + R2320/CR2320 + R2300/CR2300)/(R2140/CR2140 + R2170/CR2170 + R2210/CR2210))	1% (CRISM), 1.5% (OMEGA)	Fe/Mg - OH vibration (particularly Fe/Mg phyllosilicates)
D2300FRT	2.3 μm band depth	1 − ((R2290/CR2290 + R2320/CR2320 + R2330/CR2330 + R2305/CR2305 + R2310/CR2310)/((R2140/CR2140 + R2170/CR2170 + R2210/CR2210)*2))	Variable	
D2400	2.4 μm band depth	1 − ((R2100 + R2400)/(R2290 * 2))	1.5%	hydrated minerals; particularly polyhydrated sulfates
D2400FRT	2.4 μm band depth	1 − (((R2100 +R2210)/2 + (R2400 + R2397))/(R2290 + R2280))	Variable	

[a]R values are reflectance values at the specified wavelength and CR values are continuum removed values at the specified wavelength. FRT parameters are formulated for use with CRISM hyperspectral reflectance observations (FRT, HRL, and HRS) and other parameters are designed for use with CRISM MSP and OMEGA reflectance observations. CRISM and OMEGA spectrometers have different spectral sampling, therefore CRISM and OMEGA channels with the closest wavelength centers to those listed were utilized in parameter calculations.

Spectrally dominat hydrated and/or hydroxylated mineral phases were identified by comparing band positions of spectral absorption features in CRISM spectra with spectra of terrestrial samples contained in publically available spectral libraries (Figure 2) [*Clark et al.*, 2007; *CRISM Science Team*, 2006; *Cloutis et al.*, 2006]. Spectra contained in the libraries were typically acquired at ambient terrestrial conditions or in an environment that was purged with nitrogen for a limited amount of time. Experiments in which hydrated and/or hydroxylated mineral samples were exposed to Martian surface-like conditions for long durations showed that characteristic H_2O and/or OH related vibrational features of stable phases measured were persistent but that some absorption features, particularly H_2O related features, decreased in amplitude [*Cloutis et al.*, 2007; *Morris et al.*, 2009]. Spectral features apparent in Martian spectra are not expected to match perfectly with library spectra because multiple phases and/or phases that deviate in composition or degree of hydration from those contained in the spectral libraries likely contribute to the Martian spectra.

[24] NIR spectra are dominated by contributions from the upper 100s of micrometers of exposed materials. Spectral contrast and intensity are affected by multiple parameters that include mineralogy, grain size, and surface texture. Some phases are spectrally bland in the NIR (e.g., Fe-free anhydrous silicate minerals) and spectra of intimately mixed materials are nonlinear with respect to component proportions. Coatings that are not representative of the bulk mineralogy can contribute disproportionally to NIR spectra.

[25] Some hydrated and hydroxylated minerals exhibit distinctive spectral features in the NIR resulting from vibrational modes of H_2O and/or OH that can be spectrally diagnostic of the presence of a mineral or mineral group. OH related vibrations caused by bound OH commonly produce diagnostic spectral features. A broad H_2O related spectral absorption feature near 1.9 μm indicates that the H_2O molecule is present in some form in a material (e.g., trapped H_2O, absorbed H_2O, adsorbed H_2O, or bound H_2O). Therefore, spectra that exhibit a ~1.9 μm spectral absorption feature that lack other diagnostic vibrational bands are identified as hydrous materials (Figure 2a).

[26] Surfaces with spectral absorption features near 2.3 μm are evident in D2300 parameter maps (Table 2) of the study area in northern Sinus Meridiani. Phyllosilicates with Fe and/or Mg in octrahedral sites typically exhibit vibrational features caused by OH bound to Fe and/or Mg (e.g., Fe-OH and Mg-OH) near 2.3 μm whereas Al-rich phyllosilicates typically exhibit distinct Al-OH related vibrational features near 2.2 μm [e.g., *Hunt and Ashley*, 1979; *King and Clark*, 1989; *Bishop et al.*, 2008]. Spectral absorption features near 2.2 μm were not identified in current CRISM and OMEGA coverage of the study area.

[27] Saponite, an Mg-rich trioctahedral smectite, has distinct spectral absorption features near 1.39 (OH and H_2O related), 1.91 (H_2O related), 2.31 (Mg-OH vibration), and a weak feature at 2.39 μm [*Clark et al.*, 1990; *Bishop et al.*, 2002a]. The feature at 2.39 μm is caused by the presence of OH or H_2O in the mineral structure; however a band assignment has not been made [*Decarreau et al.*, 2008]. Nontronite, an Fe^{3+} dioctahedral smectite, has absorption features near 1.43, 1.91, and 2.28 (Fe^{3+}-OH vibration), and 2.4 μm [*Bishop et al.*, 2002b; *Frost et al.*, 2002]. Increased

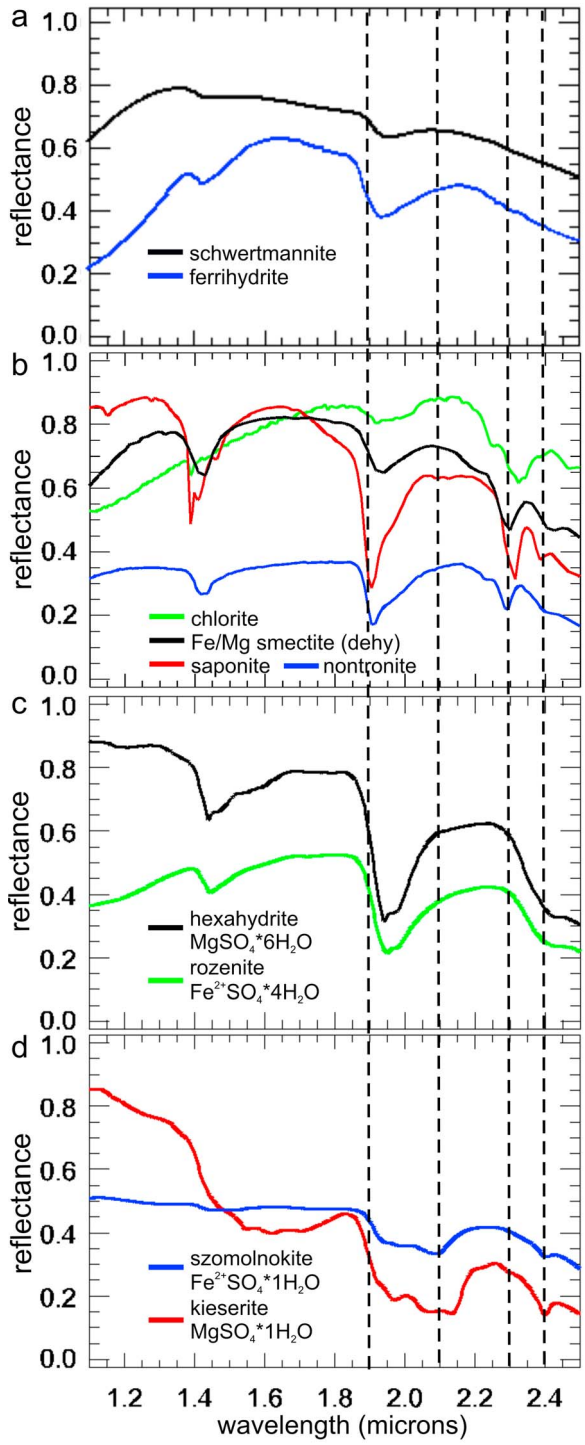

Figure 2. Laboratory reflectance spectra [*Clark et al.*, 2007; *CRISM Science Team*, 2006; *Cloutis et al.*, 2006] of selected terrestrial samples that include (a) hydrated minerals that exhibit an indistinct spectral dropoff longward of ~2.2 μm, (b) Fe, Mg, and Fe/Mg phyllosilicates, (c) Fe and Mg polyhydrated sulfates, and (d) Fe and Mg monohydrated sulfates.

proportions of Mg to Fe in smectite clays shift the ~2.3 μm band to slightly longer wavelengths [*Bishop et al.*, 2002b, *Swayze et al.*, 2002]. Chlorite is another common Fe/Mg phyllosilicate mineral group that has spectral absorption features near 1.4 and 2.3 μm [*King and Clark*, 1989]. Because chlorite contains OH but lacks H_2O in its structure, spectra of pure samples should lack an absorption feature near 1.9 μm. The ~2.3 μm Fe/Mg-OH absorption feature in several chlorite spectra contained in the USGS spectral library [*Clark et al.*, 2007] occurs at slightly longer wavelengths (between 2.32 and 2.33 μm) than the corresponding Fe/Mg-OH feature in Fe/Mg smectites (Figure 2b).

[28] Surfaces that exhibit spectral absorption features near 1.9 or 2.1 μm plus 2.4 μm are also evident in the study area in D1900, D2100, and D2400 parameter maps (Table 2). Spectra of Mg and/or Fe polyhydrated sulfate minerals, or hydrated sulfates with multiple water molecules per unit cell [*Hawthorne et al.*, 2000], exhibit absorption features near 1.9 and 2.4 μm [*Cloutis et al.*, 2006, and references therein]. Monohydrated Mg and Fe sulfates exhibit band minima near 2.1 and 2.4 μm [*Cloutis et al.*, 2006]. Some sulfate minerals, including gypsum (Ca polyhydrated sulfate), alunite (Al hydroxylated sulfate), and jarosite (Fe^{3+} hydroxylated sulfate), exhibit spectral absorption features near 2.22 to 2.27 μm that were not identified in the study area in northern Sinus Meridiani.

[29] Overlapping H_2O absorption features can result in the appearance of a broad feature near 1.9 μm in spectra of some polyhydrated sulfate minerals. Band minima between 1.93 and 1.98 μm are commonly observed in spectra of Mg and/or Fe polyhydrated sulfates (Figure 2c) [*Cloutis et al.*, 2006]. The Mg and Fe^{2+} monohydrated sulfates kieserite and szomolnokite are members of the kieserite group and have similar structures. Spectra of naturally occurring kieserite exhibit an H_2O feature near 2.13 μm and szomolnokite spectra exhibit an H_2O feature near 2.10 μm (Figure 2d). Additional laboratory studies are needed to confirm that there is a systematic relationship between the central wavelength position of the ~2.1 μm spectral feature and the dominant cation in the kieserite group. Assignment of the ~2.4 μm feature is equivocal because a feature at this wavelength is detected in spectra of both hydrated sulfate minerals and nonsulfate hydrated phases [*Crowley et al.*, 2003; *Bishop and Murad*, 2005; *Decarreau et al.*, 2008].

3.3. Image and Topographic Data

[30] CTX images (5 m/pixel), HiRISE images (25 cm/pixel), MGS Mars Orbital Camera (MOC) [*Malin et al.*, 1992] wide-angle (WA) mosaics (230 m/pixel), Mars Odyssey Thermal Emission Imaging System (THEMIS) [*Christensen et al.*, 2004] daytime and nighttime IR scaled brightness mosaics (230 m/pixel) at 12.57 μm, MGS Mars Orbiter Laser Altimeter (MOLA) [*Smith et al.*, 2001] gridded topography mosaics (450 m/pixel), and MOLA profile point data (150 m footprint) were utilized for geomorphic and topographic analyses. CRISM spectral reflectance observations were also displayed and analyzed as three band false color composite images. Data visualization and analysis were performed using IDL/ENVI and GIS software. Map coordinates were defined in areocentric latitude and positive east longitude.

[31] Relative stratigraphic positions of materials based on embayment and superposition relationships were inferred from morphologic expression and analyses of shadowed or sunlit margins in HiRISE, CTX, and MOC images. THEMIS daytime and nighttime thermal IR scaled brightness mosaics were used to compare relative differences in material

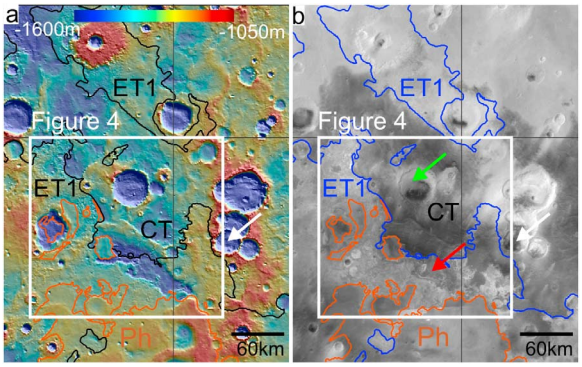

Figure 3. Context maps showing the area of northern Sinus Meridiani indicated with a black box in Figure 1. Units mapped are Cratered Terrain (CT), Etched Terrain 1 (ET1), and Plains, Hematite-bearing (Ph) (see Figure 1 caption for additional description). Locations of previously identified Fe/Mg phyllosilicates and hydrated sulfates are indicated with green and red arrows, respectively. Detailed mapping presented in Figure 4 indicates that deposits in the valley (red arrows) are stratigraphically distinct from ET1. The white arrow indicates the location of a 30 km diameter crater whose ejecta covers surrounding surfaces. (a) MOLA shaded relief map overlain by color-coded topography. (b) MOC WA mosaic.

properties. Geomorphic variations are evident in daytime images acquired in the late afternoon, partially as a result of differential solar heating. Nighttime brightness temperatures are controlled by physical properties of the surface and are dominated by thermal inertia. Reported material thicknesses were estimated from MOLA profile elevation point data.

4. Spectral and Stratigraphic Mapping in Northern Sinus Meridiani

[32] Well exposed contacts between Ph, ET1, and CT facilitate stratigraphic analyses in northern Sinus Meridiani (Figure 3). Previous analyses of OMEGA NIR spectral reflectance observations revealed monohydrated and polyhydrated sulfates in layered deposits associated with a ~120 km long northwest-southeast trending valley [*Gendrin et al.*, 2005; *Arvidson et al.*, 2005; *Griffes et al.*, 2007] and Fe/Mg phyllosilicate-bearing exposures within a 50 km diameter crater [*Poulet et al.*, 2008] (Figure 3b, red and green arrows). Our stratigraphic and spectral analyses are focused on a region in northern Sinus Meridiani located between 1°N to 5°N latitude and 3°W to 1°E longitude (Figure 4).

[33] Detailed stratigraphic, morphologic, and spectral analyses of materials within the study area are presented in sections 4.1 through 4.5 and implications of these results are discussed in section 5. We subdivided ET1 into four laterally continuous subunits, $ET1_A$, $ET1_B$, $ET1_C$, and $ET1_D$, based on the geomorphic expression of materials and their superposition relationships (Figures 4b and 4c). Layered deposits associated with the northwest-southeast trending valley located in the center of the study area that exhibit hydrated sulfate spectral signatures are distinguished from ET1 and are mapped as Layered Hydrated Sulfate (LHS) deposits. Upper layers associated with the northeastern margin of the LHS deposits are mapped as the Layered Hydrated Sulfate Cap (LHS_{cap}) (Figure 4b). The possibility that LHS_{cap} is laterally continuous with $ET1_D$ is shown in Figure 4d and is considered in section 5.2. Areas of ET1, LHS, and/or LHS_{cap} that are mantled with dark material are classified as $[ET1/LHS/LHS_{cap}]_{mantled}$ (Figure 4b).

[34] Surfaces that exhibit spectral features near 1.9, 2.1, 2.3, and 2.4 μm were identified in CRISM and OMEGA D1900, D2100, D2300, and D2400 (Table 2) parameter maps of the study area in northern Sinus Meridiani (Figure 5). Areas that appear red in Figure 5 indicate spectral features near 2.4 μm plus 1.9 μm, consistent with the presence polyhydrated sulfates; yellow areas indicate spectral features near 2.4 μm plus 2.1 μm, consistent with the presence monohydrated sulfates; and green areas exhibit a spectral feature near 2.3 μm that is typically caused by Fe/Mg-OH vibrations in Fe/Mg phyllosilicates (Figure 5).

4.1. CT, Northern Sinus Meridiani

[35] Several impact craters within CT in northern Sinus Meridiani are partially filled with high thermal inertia intracrater deposits (Figure 1c). A prominent northwest-southeast trending ridge and adjacent valley occur in the center of the study area (Figure 3a). Intercrater surfaces of CT are predominately low in albedo (Figure 3b) and are relatively smooth (Figure 6), retain small impact craters, and have polygonal fractures in some areas (Figure 6c, yellow inset). Small channel features that sometimes transition to sinuous ridges occur in CT (Figure 6c, white arrow). These sinuous ridges are similar to other features in Sinus Meridiani that were interpreted as inverted channels, or channel features that were filled with material that is more resistant to erosion than the surface into which the channel was originally incised [*Newsom et al.*, 2003; *Edgett*, 2005; *Newsom et al.*, 2010]. Channel features are buried by ET1 (Figure 6c), which indicates that channel formation predated emplacement of ET1. Dark surfaces of CT exhibit a basaltic spectral signature (Figure 7 (bottom), FRT000099C8_d CT, location shown in Figure 8) [*Poulet et al.*, 2008].

[36] CRISM spectra extracted from previously identified Fe/Mg phyllosilicate-bearing deposits on the floor of a 50 km crater are similar to OMEGA spectra [*Poulet et al.*, 2008] and exhibit spectral absorption features centered near 1.91 and 2.31 μm, weaker features near 1.4 and 2.39 μm, and a shoulder near ~2.24 μm (Figure 7, FRT0000960F). Spectral features at 1.91, 2.31, and 2.39 μm are consistent with contributions from Mg-rich smectite (Figure 2b). The shape of the 2.31 band and the shoulder near ~2.24 μm may result from the presence of chlorite in addition to Mg-rich smectite (Figure 2b). Alternatively, the shoulder near ~2.23 μm could be produced from Al-OH vibrations resulting from substitution of Al into octahedral sites in the smectite [e.g., *King and Clark*, 1989]. Additional exposures that exhibit spectral absorption features near 2.3 μm are detected in CT in CRISM image FRT000099C8 on and to the north of rampart [*Barlow et al.*, 2000] ejecta from a 16 km diameter impact crater (Figure 8). Spectral features centered near 1.92 and 2.30 to 2.31 μm and weaker features at ~1.4 and 2.39 μm (Figure 7, FRT00099C8) are consistent with the presence of Fe/Mg smectites (Figure 2b).

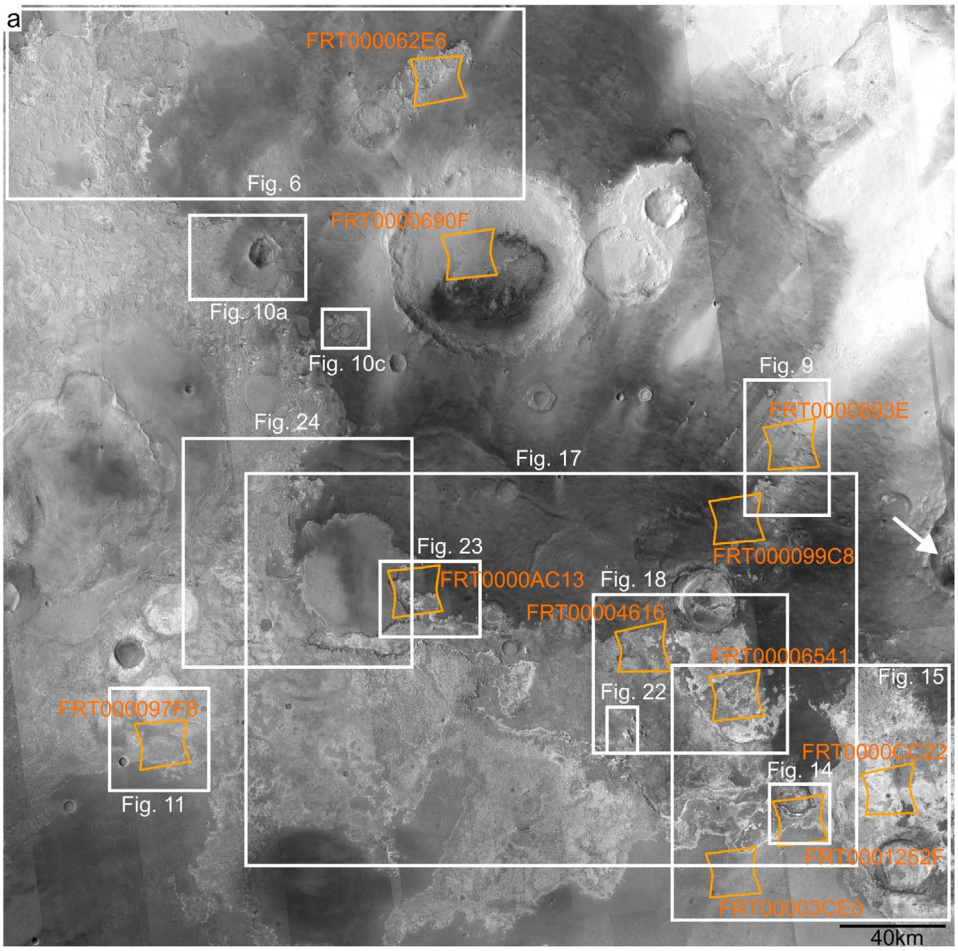

Figure 4. (a) CTX mosaic of the study area (1°N to 5°N, 3°W to 1°E) in northern Sinus Meridiani indicated with a white box on the context maps shown in Figure 3. Footprints of CRISM FRT images shown in this paper are outlined and labeled in orange. The white arrow indicates the location of a 30 km diameter crater from which dark material, inferred to be crater ejecta, that is visible on surrounding surfaces appears to have originated. (b) CTX mosaic of the study area (1°N to 5°N, 3°W to 1°E) in northern Sinus Meridiani with a detailed units map overlain. Cratered Terrain (CT) occurs at the base of the stragitgraphic sequence and is unconformably overlain by Etched Terrain 1 (ET1). Intracrater deposits within CT are not distinguished for simplicity. The bedrock and unconsolidated components of the Plains, Hematite-bearing (Ph) are mapped as Etched Terrain 2 (ET2) and the Plains Mantle, Hematite-bearing (Pm), respectively. ET1 is subdivided into four stratigraphically distinct subunits: $ET1_A$, $ET1_B$, $ET1_C$, and $ET1_D$ (Table 1). Layered Hydrated Sulfate (LHS) deposits and the Layered Hydrated Sulfate Cap (LHS_{cap}) associated with the valley in the center of the study area are distinguished from ET1. Mantled areas of ET1, LHS, and/or LHS_{cap} are classified as $[ET1/LHS/LHS_{cap}]_{mantled}$. The white arrow indicates the location of a 30 km diameter crater from which dark material, inferred to be crater ejecta, that is visible on surrounding surfaces appears to have originated. Footprints of CRISM FRT images that are labeled in Figure 4a are outlined in white. (c) Stylized vertical cross sections showing inferred stratigraphic sequences at locations A, B, C, and D (indicated in Figure 4b). Vertical sections labeled 1 and 2 represent two possible stratigraphic columns that are consistent with the units map at the specified locations. Contact types between units are not rendered in these stylized vertical cross sections. (d) Alternate version of the portion of the units map outlined with a black box in Figure 4b in which LHS_{cap} and $ET1_D$ are part of the same laterally continuous unit.

4.2. $[ET1/LHS/LHS_{cap}]_{mantled}$ Description

[37] Where well exposed, surfaces of ET1, LHS, and LHS_{cap} have intermediate albedos and relatively high thermal inertias (Figures 1c and 3b and Table 1). Some portions of ET1, LHS, and LHS_{cap} are mantled by low-albedo, relatively low thermal inertia material. Where the dark mantle covers small areas, the unit underlying the mantle can be inferred from surrounding exposures. However, in areas

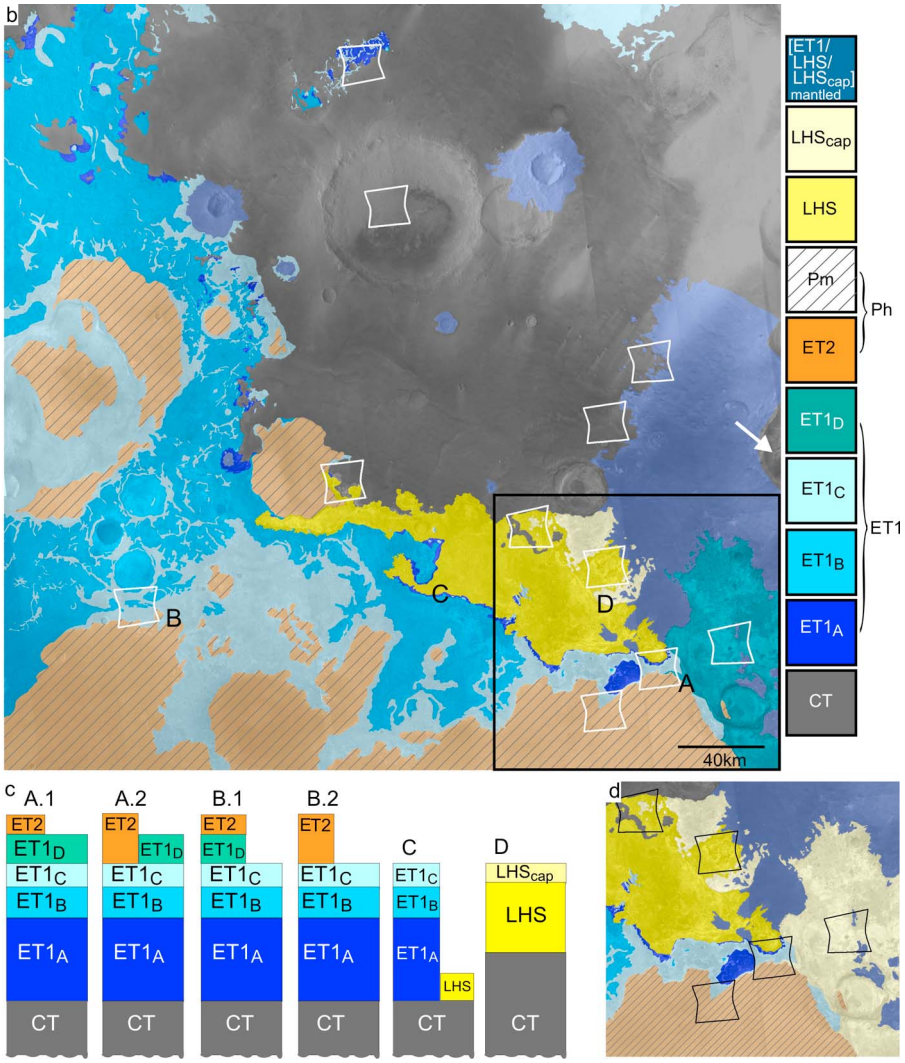

Figure 4. (continued)

where the mantle is relatively extensive, identification of the underlying unit (e.g., $ET1_A$, $ET1_B$, $ET1_C$, $ET1_D$, LHS, or LHS_{cap}) is difficult. Therefore, mantled areas that are laterally continuous with or occur at similar stratigraphic levels as $ET1_A$, $ET1_B$, $ET1_C$, $ET1_D$, LHS, or LHS_{cap} were classified as $[ET1/LHS/LHS_{cap}]_{mantled}$ and specific assignment of the unit(s) underlying the mantle was not made (Figure 4b).

[38] The dark mantle material commonly occurs in the vicinity of impact craters deep enough to have excavated and emplaced underlying CT as ejecta deposits on surrounding surfaces. The dark mantle component of $[ET1/LHS/LHS_{cap}]_{mantled}$ located in the eastern portion of the study area adjacent to a 30 km diameter impact crater appears to have originated as ejecta from this crater (Figures 3 and 4, white arrow). High thermal inertia light-toned layers that stand ~200 m above CT are visible in exposures along the western margin of this mantled area (Figure 9). Continuous ejecta deposits mantle ET1 shown in Figure 10a and remnants of dark ejecta mantle the surface of ET1 shown in Figure 10c.

4.3. ET1, Northern Sinus Meridiani

[39] Multiple outliers of ET1 that are separated by 10s of kilometers from larger exposures occur in northern Sinus Meridiani (Figure 3). The smallest outliers of ET1 surround craters and may have been armored from erosion by crater ejecta deposits, resulting in pedestal-like craters (Figure 4b). The presence of outliers of ET1 suggests that substantial differential erosion of ET1 occurred in this region [*Hynek and Phillips*, 2001; *Hynek et al.*, 2002].

[40] Four geomorphically distinct subunits of ET1 ($ET1_A$, $ET1_B$, $ET1_C$, and $ET1_D$) were identified in the study area in northern Sinus Meridiani (Figure 4b). $ET1_A$ is the stratigraphically lowest subunit within ET1 and $ET1_D$ is the stratigraphically highest subunit (Figure 4c). $ET1_A$, $ET1_B$, and $ET1_C$ are consistently exposed in the southern and western portion of the study area and in outliers of ET1 that occur to the north (Figure 4b). $ET1_D$ is exposed in the eastern portion of the study area (Figure 4b). Subunits are

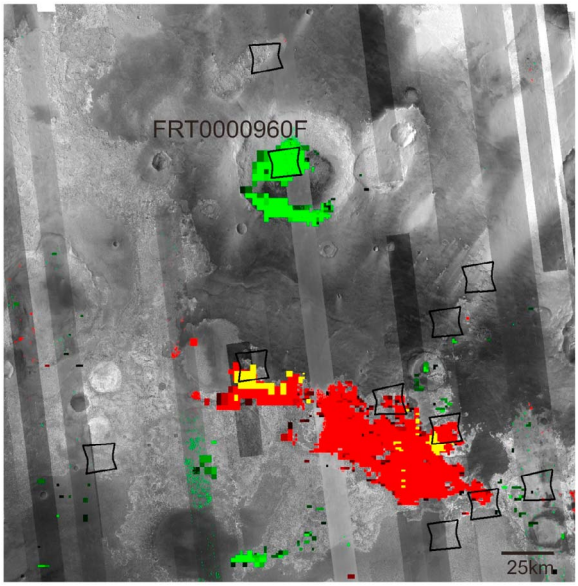

Figure 5. CTX mosaic shown in Figure 4a with CRISM (MSP and MSW) and OMEGA parameters maps (Table 2) overlain. Red areas exhibit high D1900 and D2400 parameter index values that indicate spectral features at ~1.9 and 2.4 μm, consistent with the presence of polyhydrated sulfates. Yellow areas exhibit high D2100 and D2400 parameter index values that indicate spectral features at ~2.1 and 2.4 μm, consistent with the presence of monohydrated sulfates. Green areas exhibit a high D2300 parameter index value that indicates the presence of a feature at ~2.3 μm that is typically caused by Fe/Mg-OH vibrations in Fe/Mg phyllosilicates. Areas that exhibit high D1900 parameter index values but that lack additional distinctive absorption features at longer wavelengths (i.e., hydrated materials that were not identified as hydrated sulfates or Fe/Mg phyllosilicates) are not shown on this parameter map (see Figure 1d hydration map). OMEGA coverage varies in spatial resolution from ~400 to 2500 m/pixel and spatial registration of OMEGA images with the CTX base map is imperfect. CRISM MSP (200 m/pixel) and MSW (100 m/pixel) 1.1 μm images are overlain on the CTX mosaic to indicate CRISM multispectral coverage. Footprints of CRISM FRT images detailed in this paper are shown with black outlines (FRT parameter maps are not overlain).

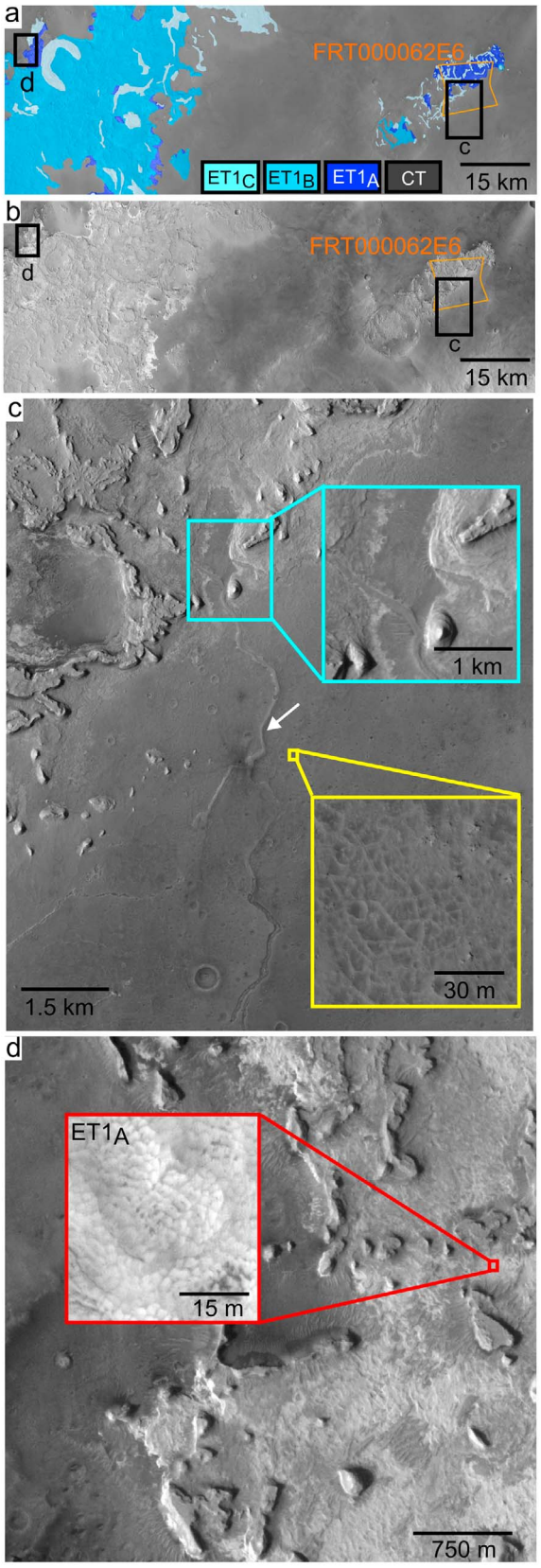

Figure 6. (a) Subset of the units map (Figure 4b) showing CT and eroded portions of ET1; location labeled in Figure 4a. (b) CTX mosaic. (c) Higher-resolution view (subset of CTX image P03_002390_1840). The portion of the channel feature indicated with a white arrow is inverted, or has positive relief. The yellow inset shows an area in CT that exhibits polygonal fracturing (subset of HiRISE image PSP_004091_1845). Layers of $ET1_A$, $ET1_B$, and $ET1_C$ are visible in mesa walls in the cyan inset (subset of HiRISE image PSP_004091_1845). (d) Higher-resolution view (subset of CTX image P06_003379_1827). Mesas that consist of $ET1_A$, $ET1_B$, and $ET1_C$ are located near the edge of a large, continuous expanse of ET1. The red inset shows the distinctive scalloped texture of $ET1_A$ (subset of HiRISE image PSP_003946_1850).

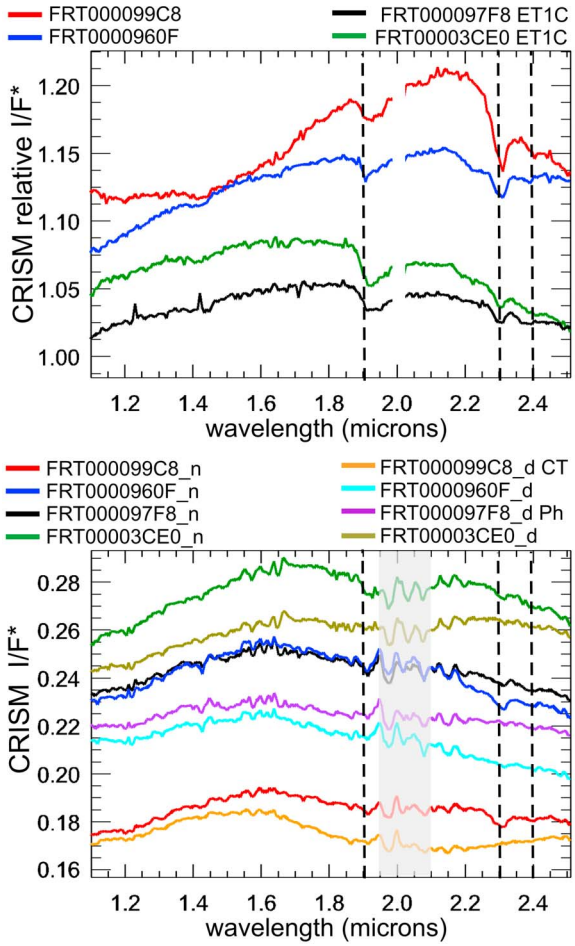

Figure 7. (top) CRISM relative reflectance spectra extracted from areas of selected FRTs with Fe/Mg phyllosilicate-like spectral signatures. (bottom) CRISM *I*/*F** (volcano scan and cos(*i*) corrected CRISM *I*/*F*) numerator (_n) and denominator (_d) spectra that were used to generate the ratio spectra shown in the top plot. Residual atmospheric features are likely to occur in the region of the spectrum highlighted in gray in which intense atmospheric CO_2 absorptions occur. Each spectrum is the average of 25 spectra.

described in reverse stratigraphic order with the exception that $ET1_D$ is presented last.

[41] $ET1_C$ commonly exhibits a distinctive knob to ridged morphology that is visible at intermediate spatial scales (hundreds of meters) (Figure 11 and Table 1). Ridges within ET1 were previously recognized in Sinus Meridiani [e.g., *Arvidson et al.*, 2003; *Edgett*, 2005; *Salvatore et al.*, 2008]. Analyses of CTX images show that the knobs and ridges are traceable to more continuous material that is preserved near the margin of overlying Ph (Figure 11c). Thus, the knob and ridges appear to be an erosional morphology of $ET1_C$. The thickness of $ET1_C$ is difficult to determine because it caps ridges whose walls may consist of stratigraphically lower materials. $ET1_C$ is estimated to have a thickness of 10 to 30 m (Figure 11b, MOLA profile). A spectral absorption feature near 2.3 μm is detected in some exposures of $ET1_C$ located in the southwestern portion of the study area (Figure 5, green pixels). Spectra extracted from the surface of $ET1_C$ covered by CRISM image FRT000097F8 (Figure 12) exhibit spectral absorption features centered near 1.92, 2.30 to 2.31 μm, and 2.39 μm (Figure 7, FRT000097F8 $ET1_C$), consistent with the presence of Fe/Mg smectite (Figure 2b).

[42] $ET1_B$ occurs stratigraphically below $ET1_C$ and is exposed in surfaces intervening remnant knobs and ridges of $ET1_C$ (Figure 11 and Table 1). $ET1_B$ is relatively smooth at intermediate and small (10s of meters) spatial scales (Figure 11e) and appears brighter than $ET1_C$ (Figure 11c). The thickness of $ET1_B$ is estimated at 40 to 60 m. Spectra of $ET1_B$ extracted from FRT000097F8 (Figure 11) exhibit a shallow H_2O related absorption feature near 1.92 μm and an indistinct spectral dropoff at wavelengths longward of ~2.2 μm (Figure 13, FRT000097F8 $ET1_B$). This spectral shape is consistent with spectra of hydrated phases that include hydrous hydroxides and some hydrated ferric sulfates (Figure 2a). A small exposure of material with spectral features near ~1.9 and 2.4 μm, indicative of the presence of polyhydrated sulfates, is also detected in FRT000097F8 (Figure 12b, magenta pixels). This spectral signature is not representative of $ET1_B$ and will be discussed in section 4.5.

[43] $ET1_A$ is the stratigraphically lowest subunit of ET1 and is exposed in heavily eroded areas that include plateau

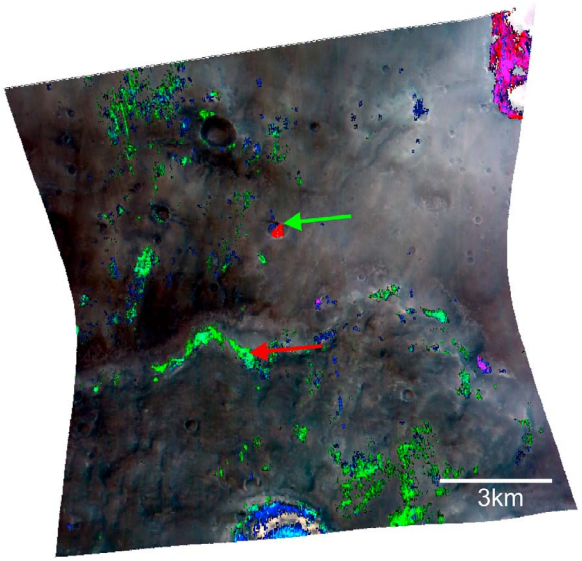

Figure 8. False color composite (R, 2.5; G, 1.5; B, 1.1 μm) of CRISM image FRT000099C8 (location shown in Figures 4a and 9) with parameter map color composite overlain (R, D2400FRT (2% linear stretch 0.012–0.022); G, D2300FRT (2% linear stretch 0.005–0.010); B, D1900FRT (2% linear stretch 0.015–0.025)) (Table 2). Blue areas exhibit high D1900FRT parameter values consistent with the presence of hydrated materials, magenta areas exhibit high D1900FRT and D2400FRT parameter values indiciative of polyhydrated sulfates, red areas exhibit high D2400FRT and D2100FRT (not shown) parameter values indicative of monohydrated sulfates, and green areas exhibit high D2300FRT parameter values indicative of Fe/Mg phyllosilicates. Spectra extracted from the locations indicated with the red and green arrows are shown in Figure 7 (FRT000099C8) and Figure 26 (FRT000099C8 mono), respectively.

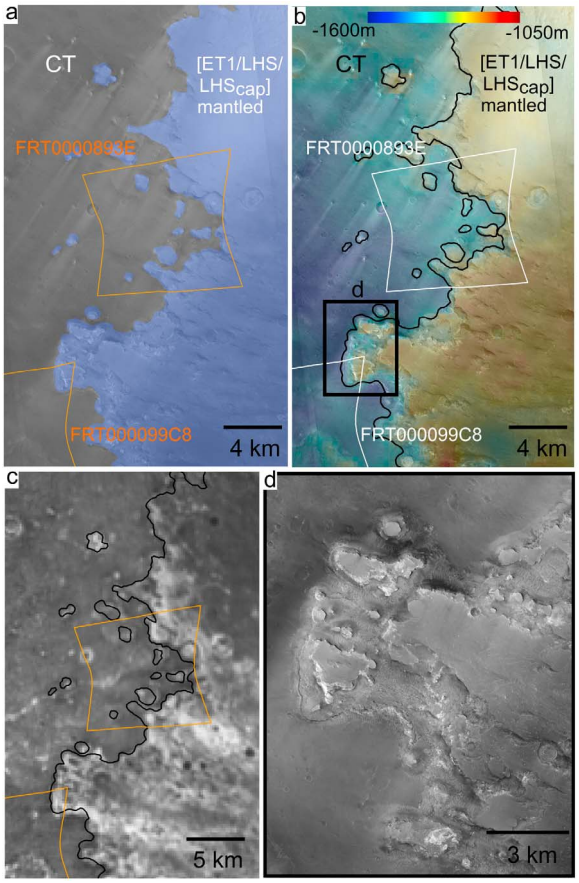

Figure 9. (a) Subset of the units map (Figure 4b) showing the contact between CT and $[ET1/LHS/LHS_{cap}]_{mantled}$; location labeled in Figure 4a. Footprints of CRISM images FRT000099C8 (shown in Figure 8) and FRT0000893E (shown in Figure 25) are overlain in white. $[ET1/LHS/LHS_{cap}]_{mantled}$ is ~3 crater radii from the center of the 30 km impact crater indicated with a white arrow in Figures 3a and 4a and stands up to ~200 m above the surface of CT. At a distance of three crater radii, initial ejecta deposition of <10 m thick is expected [*McGetchin et al.*, 1973; *Garvin and Frawley*, 1998]. (b) CTX mosaic with MOLA color-coded topography overlain. (c) THEMIS NIR mosaic. Relatively high thermal inertia areas appear bright. (d) Higher-resolution view of area outlined in black (Figure 9b) showing light-toned material exposed along the margin of $[ET1/LHS/LHS_{cap}]_{mantled}$ (subset of CTX image P13_005937_1834).

or mesa walls and low regions surrounding mesas (Figures 6 and 14 and Table 1). $ET1_A$ has a higher albedo than both $ET1_B$ and $ET1_C$ and exhibits a distinctive scalloped texture that is visible in HiRISE images (Figures 6d and 14b, red insets). Scalloped textured terrain that has a broadly similar morphology to $ET1_A$ at HIRISE resolution, but that occurs in low thermal inertia (e.g., dusty) areas, was analyzed by *Bridges et al.* [2010]. The thickness of $ET1_A$ is variable and appears to be controlled by the underlying topography of CT. The thickest exposures of $ET1_A$ (~150 m thick) occur in the scarp wall located along the southern margin of the northeast-southwest trending valley (Figure 4b). $ET1_A$ is well exposed in a portion of the scarp wall covered by CRISM image FRT0001252F (Figure 14c). Spectra extracted from $ET1_A$ are relatively bland between 1.0 and 2.5 μm and do not exhibit obvious H_2O and/or OH related vibrational features (Figure 13, FRT0001252F $ET1_A$).

[44] $ET1_D$ is identified in the eastern portion of the study area and occurs stratigraphically above $ET1_C$ (Figure 15 and

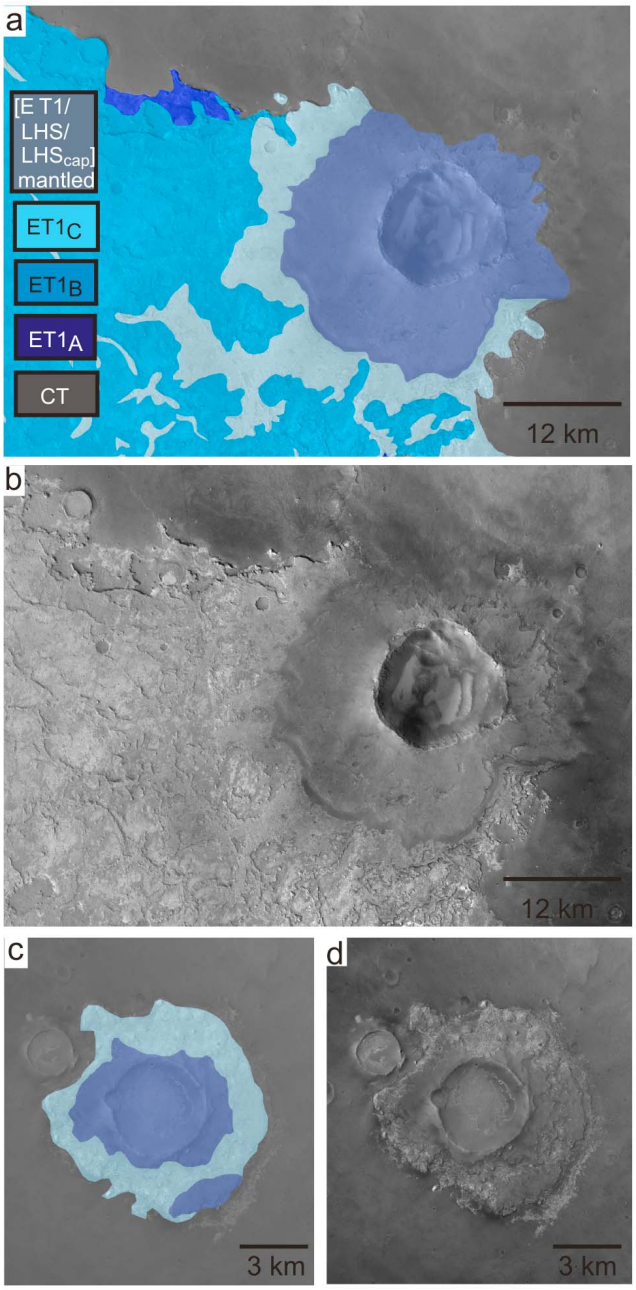

Figure 10. Dark material surrounding craters that appears to have originated as crater ejecta mantles higher-albedo ET1 (locations indicated in Figures 4a and 4b).

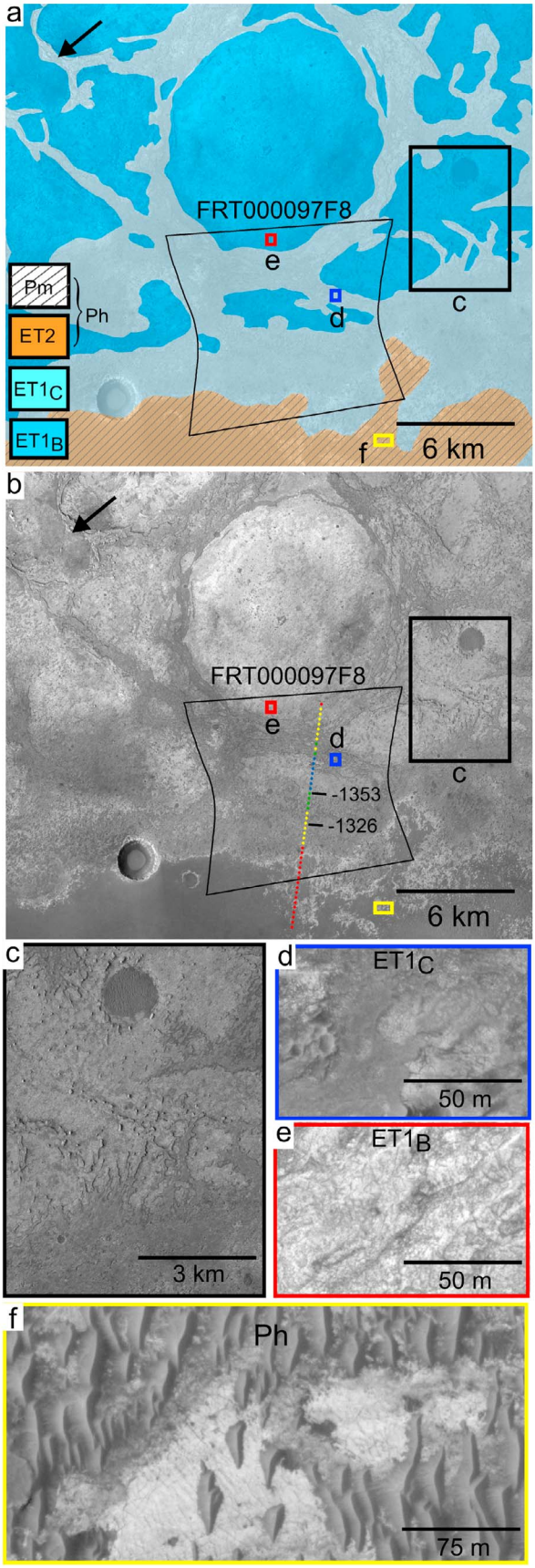

Table 1). Multiple strata within $ET1_D$ are exposed along a ~70 m topographic rise that occurs near the margin between $ET1_C$ and $ET1_D$ (Figure 15d). The margin between $ET1_D$ and ET2 is difficult to define (Figure 15d). $ET1_D$ appears to underlie ET2 and may occur in the area labeled "$ET1_D$?" in Figure 15d. The interpretation that $ET1_D$ underlies ET2 is based on analysis of a small interval of material and is not definitive; it is possible that $ET1_D$ embays ET2 (Figure 4c, vertical section A2). Spectra extracted from two layers within $ET1_D$ in CRISM image FRT0000CC22 (Figure 16) exhibit pronounced H_2O related absorptions features near 1.92 μm and an indistinct spectral dropoff at wavelengths longward of ~2.2 μm (Figure 13, FRT0000CC22 $ET1_D$ 1 and FRT0000CC22_$ET1_D$ 2) that is consistent with spectra of hydrated phases including hydrous hydroxides and some hydrated ferric sulfates (Figure 2a). Similar spectral shapes are observed in ET1 located to the east of the study area [*Poulet et al.*, 2008]. Polyhydrated sulfate spectral signatures were detected along the margin of low-albedo mantle in FRT0000CC22 (Figure 16b, magenta pixels) and in the area indicated with a black arrow in FRT0001252F (Figure 14c) that corresponds to the material labeled $ET1_D$? in Figure 15d. These materials are discussed in section 4.5.

4.4. LHS and LHS_{cap}

4.4.1. LHS and LHS_{cap} Descriptions

[45] Layered Hydrated Sulfate (LHS) deposits are exposed on the floor of the northwest-southeast trending valley located in the center of the study area and within higher-elevation exposures near the northeastern margin of the valley (Figures 17 and 18). LHS deposits exhibit spectral absorptions features near 2.1 plus 2.4 μm and ~1.9 plus 2.4 μm, indicative of the presence of monohydrated and polyhydrated sulfates, respectively (Figure 5, yellow and red pixels). Polyhydrated sulfates are spectrally dominant over a large area of the valley floor and monohydrated sulfates occur on the western portion of the valley floor and in higher-elevation, plateau-forming exposures in the northeastern portion of the LHS deposits (Figures 5 and 17b) [*Griffes et al.*, 2007]. Analyses of high-resolution CRISM, CTX, and HiRISE images reveal that layers containing monohydrated sulfates are intercalated with polyhydrated layers near the northeastern margin of the LHS deposits (Figures 19 and 20). Hydrated sulfate spectral signatures are detected in both low- and high-albedo layers within the LHS deposits (Figure 19). Pits and grooves are visible in LHS deposits at small to intermediate spatial scales (Figure 19d).

Figure 11. (a) Subset of the units map (Figure 4b) showing $ET1_B$, $ET1_C$, and Ph; location indicated in Figure 4a. A low ridge capped by $ET1_C$ is indicated with a black arrow. (b) CTX mosaic. Selected MOLA profiles points are shown (elevation range between −1368 and −1318 m). (c) A knobby portion of $ET1_C$ transitions to a more continuous layer (subset of CTX image P04_002746_1808). $ET1_B$ is visible on surfaces intervening knobs and ridges of $ET1_C$. (d–f) Subsets of HiRISE image PSP_007572_1820 showing the small-scale morphology of $ET1_C$, $ET1_B$, and ET2.

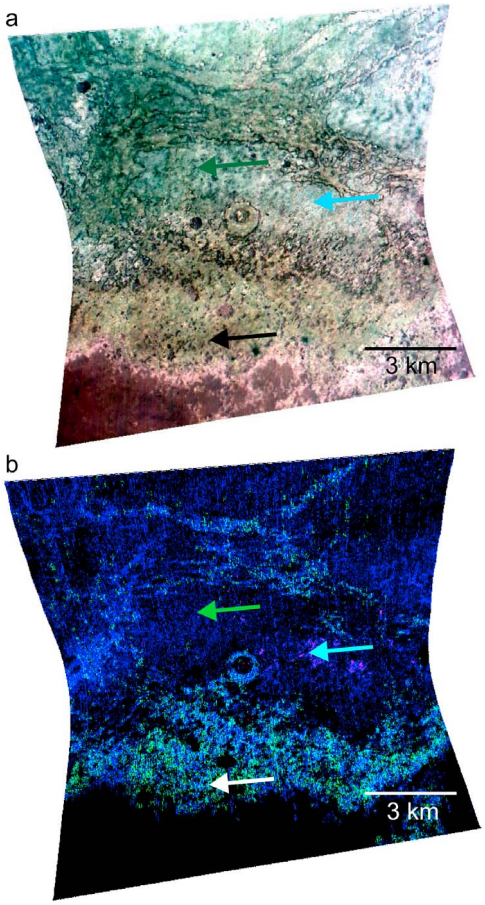

Figure 12. CRISM image FRT000097F8 (footprint shown in Figure 11) mainly covering $ET1_C$ and $ET1_B$ with Ph exposed in the southwestern portion of the image. Black, green, and cyan arrows indicate locations of spectra extracted from $ET1_C$ (Figure 7 FRT000097F8 $ET1_C$), $ET1_B$ (Figure 13 FRT000097F8 $ET1_B$), and a spectrally anomalous area indicated by magenta pixels (Figure 26 FRT000097F8 poly). (a) False color composite (R, 2.5; G, 1.5; B, 1.1). (b) Parameter map color composite (R, D2400FRT (2% linear stretch 0.010–0.020); G, D2300FRT (2% linear stretch 0.003–0.008); B, D1900FRT (2% linear stretch 0.012–0.022)) (Table 2). Blue areas exhibit high D1900FRT parameter values consistent with the presence of hydrated materials, magenta areas exhibit high D1900FRT and D2400FRT parameter values indicative of polyhydrated sulfates, and cyan areas exhibit high D2300FRT and D1900FRT parameter values indicative of Fe/Mg phyllosilicates.

[46] CRISM spectra extracted from areas with high D1900 and D2400 parameter values in FRT00004616 exhibit broad spectral absorption features centered near 1.94 μm and a reflectance drop off longward of ~2.3 μm with a band minimum near 2.39 to 2.40 μm (Figure 21, FRT00004616 LHS poly) that is spectrally consistent with the presence of Mg and/or Fe polyhydrated sulfates (Figure 2c). CRISM spectra extracted from areas with high D2100 and D2400 parameter values exhibit a spectral absorption feature centered near 2.13 μm and a reflectance drop off longward of ~2.3 μm with a well defined band minimum near 2.40 μm (Figure 21, FRT00004616 LHS mono). Although a band centered at 2.13 μm is more consistent with spectra of the Mg monohydrated sulfate kieserite than spectra of the Fe monohydrated sulfate szomolnokite (Figure 2d), the relationship between the wavelength center of the spectral feature near ~2.1 μm and cation in the kieserite group is not well established. CRISM spectra extracted from LHS deposits also typically exhibit a broad spectral absorption feature centered near ~1 μm (Figure 21). This electronic feature could arise from the presence of ferrous hydrated sulfate

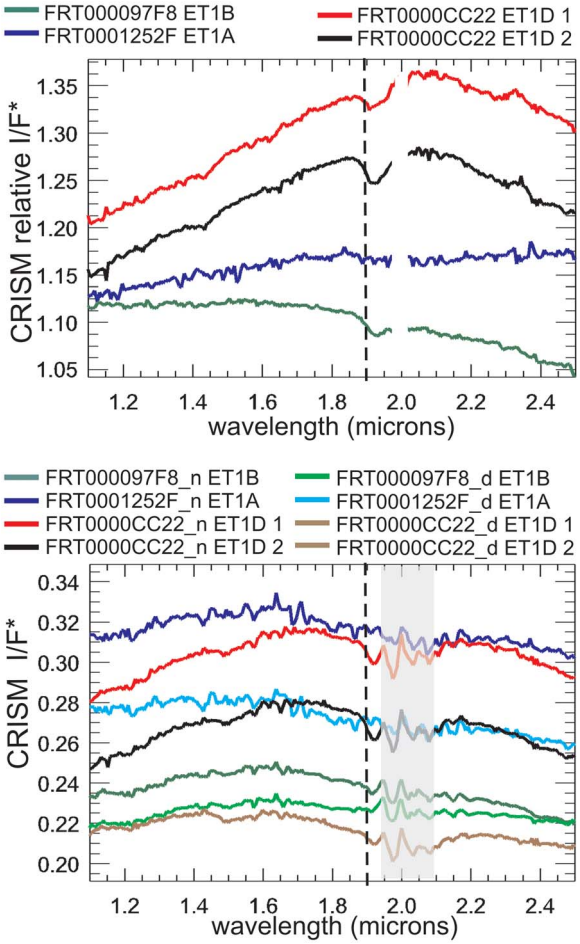

Figure 13. (top) CRISM relative reflectance spectra extracted from areas of selected FRTs that exhibit hydration features at 1.9 μm but lack additional diagnostic vibrational features at longer wavelengths or are spectrally bland. The red spectrum was offset by −0.10, and the green spectrum offset by 0.05 for clarity. (bottom) CRISM I/F^* (volcano scan and cos(i) corrected CRISM I/F) numerator (_n) and denominator (_d) spectra that were used to generate the ratio spectra shown in the top plot. Residual atmospheric features are likely to occur in the region of the spectrum highlighted in gray in which intense atmospheric CO_2 absorptions occur. Each spectrum is the average of 25 spectra.

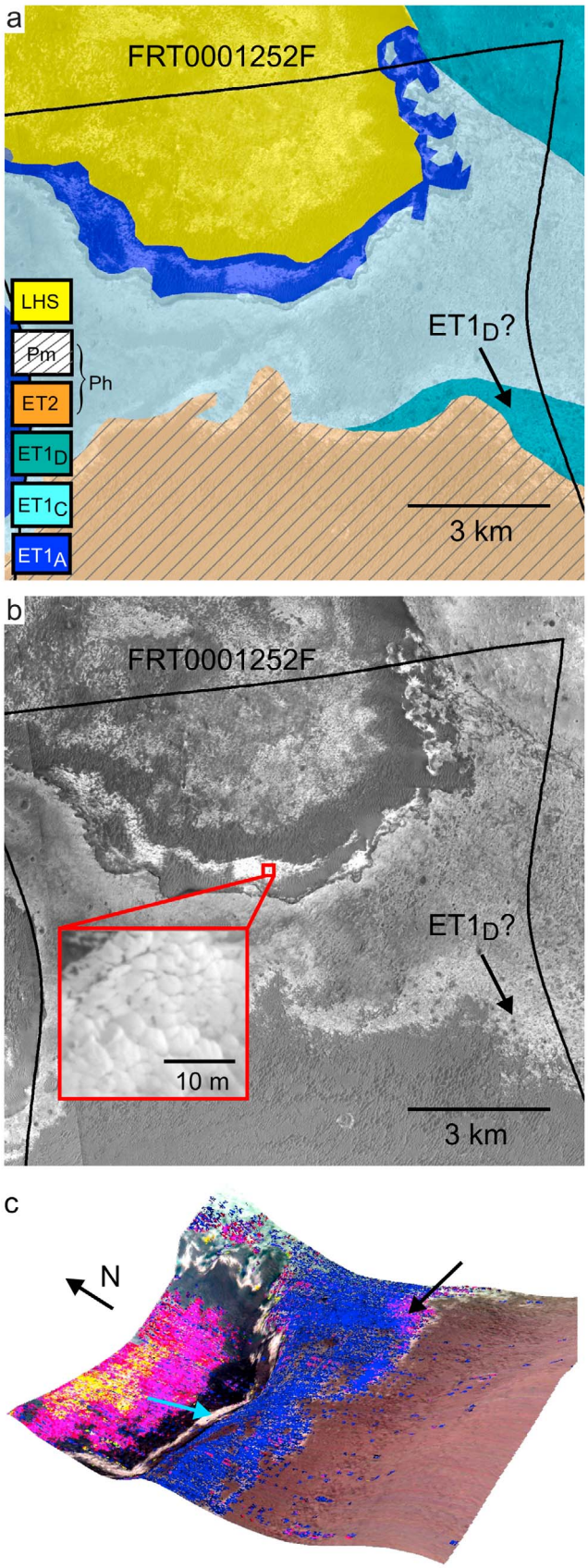

minerals or from contributions by other ferrous hydrous or anhydrous phases that occur in the CRISM pixels from which the spectra were extracted. Low-albedo aeolian deposits that have a basaltic spectral signature similar to spectrum FRT000099C8_d CT shown in Figure 7 (bottom) are observed in the valley (e.g., Figure 14b).

[47] The LHS_{cap} occurs on plateau surfaces (Figure 18) and is higher in albedo and smother at intermediate spatial scales than LHS deposits (Figure 19d). Spectra extracted from LHS_{cap} shown in FRT00004616 (Figure 19) exhibit an H_2O related feature at 1.92 μm but do no exhibit a well defined spectral absorption feature near 2.4 μm (Figure 21, FRT00004616 LHS_{cap}). Spectra of LHS_{cap} are distinct from spectra of LHS deposits and are consistent with spectra of hydrated phases that include hydrous hydroxides and some hydrated ferric sulfates (Figure 2a).

4.4.2. Stratigraphic Analyses of LHS and LHS_{cap}

[48] A ~200 m section of ET1 is exposed along the southern margin of the LHS deposits in which both steep faces and more gradual slopes are observed (Figure 17). Hydrated sulfate spectral signatures are not identified in existing high-resolution CRISM coverage of the scarp wall. Instead, hydrated sulfates are identified in LHS deposits that occur on the valley floor (Figure 14c). $ET1_A$ is visible at the base of the section of ET1 exposed in the southern scarp wall (Figures 14b and 17). The configuration of the southern margin of the valley suggests that the LHS deposits either underlie or embay $ET1_A$, however aeolian debris obscures contacts (Figure 14b) making it difficult to determine the stratigraphic relationship between LHS deposits and $ET1_A$. Mesas with the same sequence of layers observed in the cliff wall ($ET1_A$, $ET1_B$, and $ET1_C$) occur near the center of the valley (Figure 22). Contacts between LHS and $ET1_A$ within

Figure 14. (a) Subset of the units map (Figure 4b) showing exposures of $ET1_A$ in the scarp wall along the margin of LHS deposits; location indicated in Figure 4a. (b) CTX mosaic. The red inset shows the distinctive scalloped morphology of $ET1_A$ exposed in the cliff wall (subset of HiRISE image PSP_001493_1815). (c) CRISM image FRT0001252F false color composite (R, 2.5; G, 1.5; B, 1.1 μm) with parameter map color composite (R, D2400FRT (2% linear stretch 0.010–0.015); G, D2100FRT (2% linear stretch 0.015–0.025); B, D1900FRT (2% linear stretch 0.012–0.020)) (Table 2) overlain and draped on MOLA topography (vertical exaggeration is 10). Blue areas exhibit high D1900FRT parameter values consistent with the presence of hydrated materials, magenta areas exhibit high D1900FRT and D2400FRT parameter values indicative of polyhydrated sulfates, and yellow areas exhibit high D2100FRT and D2400FRT parameter values indicative of monohydrated sulfates. $ET1_A$ does not exhibit evidence for the presence of hydrated phases. LHS deposits exhibit strong monohydrated and polyhydrated sulfate spectral signatures. A weak polyhydrated sulfate signature is detected in rock near the base of ET2 that is indicated with a black arrow (higher-resolution view is shown in Figure 15d). The blue arrow indicates the location of a spectrum extracted from $ET1_A$ (Figure 13, FRT0001252F $ET1_A$).

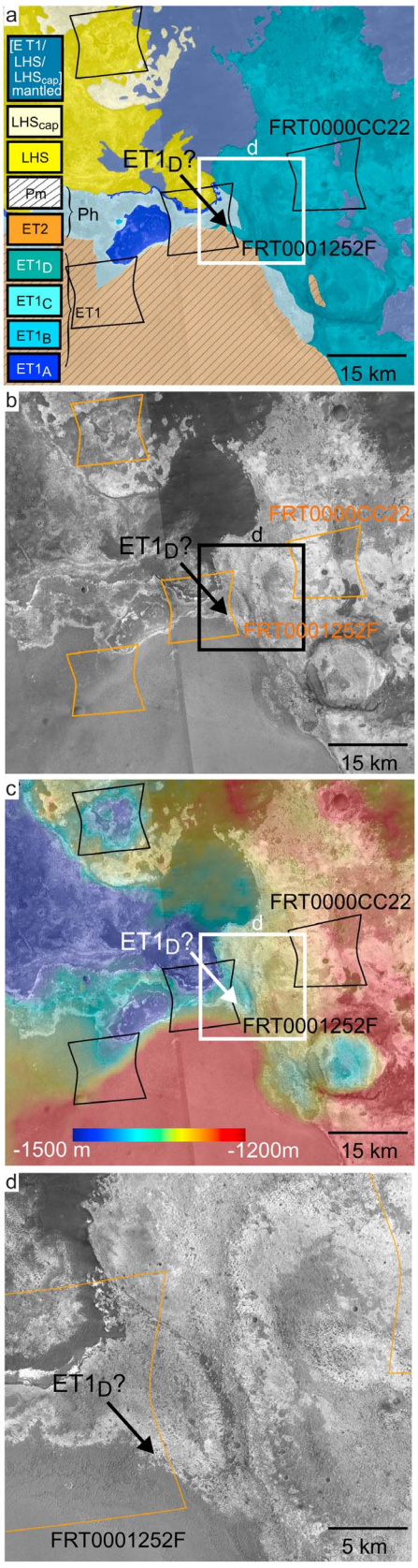

these mesas are well defined. Based on analysis of these contacts, we conclude that LHS deposits on the valley floor embay $ET1_A$ (Figure 22).

[49] Exposures along the northern margin of the LHS deposits show that LHS deposits occur stratigraphically above CT. LHS deposits embay and partially cover rampart ejecta from a preexisting crater in CT (Figures 18 and 19). LHS deposits also embay a channel feature eroded into the surface of CT that extends to the north and cuts a northwest-southeast trending ridge (Figures 17c). This embayment and crosscutting relationship establishes that emplacement of LHS deposits postdates the formation of the ridge within CT.

[50] Layers in the LHS deposits terminate in low mesas along their northwestern margin (Figure 23). High-albedo material is exposed at the base of the low mesas (Figure 23). Some exposures of the underlying light-toned material have the distinctive scalloped morphology characteristic of $ET1_A$ (Figure 23c). Analyses of CRISM spectra in conjunction with higher-resolution CTX and HiRISE images indicate that these areas do not exhibit distinctive hydrated sulfate spectral signatures (Figure 23).

[51] LHS_{cap} occurs stratigraphically above LHS (Figures 18 and 19). Outliers of LHS_{cap} that are visible on small mesa surfaces adjacent to larger exposures of LHS_{cap} indicate that LHS_{cap} was originally more extensive (Figure 18d). Multiple layers in the LHS deposits are exposed in areas surrounding LHS_{cap}, with higher-elevation layers occurring closest to the LHS_{cap}. Analysis of HiRISE anaglyph PSP_002680_1825_PSP_003392_1825, which covers deposits shown in Figure 19d, does not reveal obvious deformation textures or steeply dipping beds. Instead layers at multiple elevations within the LHS deposits appear to be exposed as a result of differential erosion.

4.5. Additional Hydrated Sulfate Exposures in Northern Sinus Meridiani

[52] Exposures that exhibit hydrated sulfate spectral signatures are not restricted to LHS deposits. Polyhydrated sulfates occur in a topographic low to the northwest of the LHS deposits and small exposures with monohydrated and polyhydrated sulfate spectral signatures were identified to the north and northeast of LHS deposits in low areas near the bases of high-standing outcrops in two locations. Polyhydrated sulfate spectral signatures are also detected in limited exposures on high-standing surfaces of ET1 located to the southwest, south, and east of the LHS deposits.

Figure 15. (a) Subset of the units map (Figure 4b) showing the contact between $ET1_C$ and $ET1_D$; location indicated in Figure 4a. (b) CTX mosaic. The contact between $ET1_D$ and LHS_{cap} is obscured by intervening $[ET1/LHS/LHS_{cap}]_{mantled}$, making it difficult to determine the stratigraphic relationship between $ET1_D$ and LHS_{cap}. (c) CTX mosaic with MOLA color-coded topography overlain. (d) Higher-resolution view (subset of CTX image P13_005937_1834) showing layers in $ET1_D$. Rock near the base ET2 indicated with a black arrow may be part of $ET1_D$.

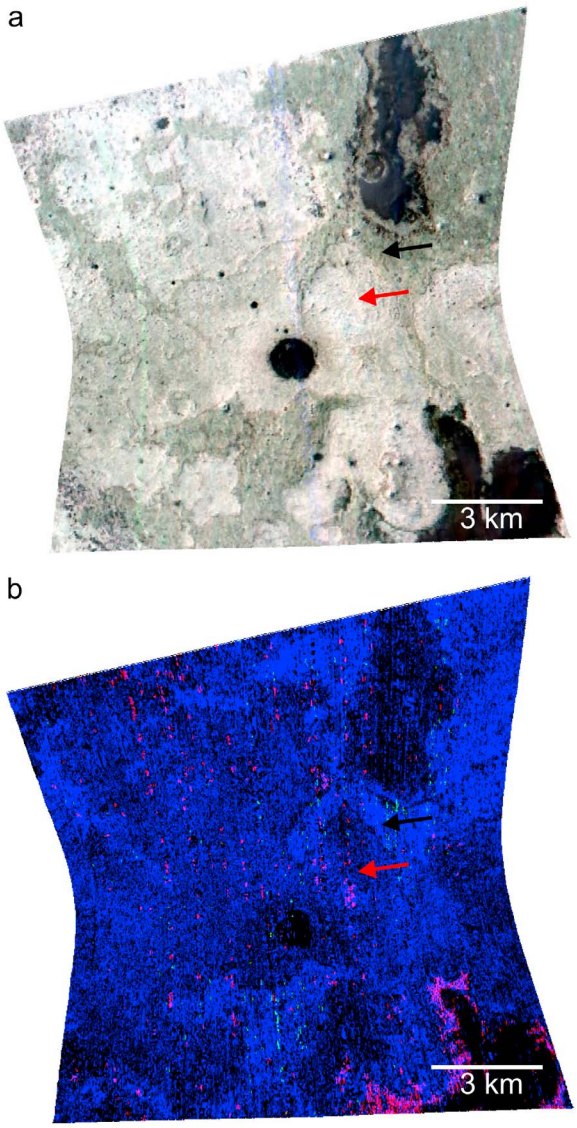

Figure 16. CRISM image FRT0000CC22 (footprint shown in Figure 15) showing $ET1_D$. The red and black arrows indicate locations of spectra extracted from $ET1_D$ shown in Figure 13 (FRT0000CC22 $ET1_D$ 1 and FRT0000CC22 $ET1_D$ 2). (a) False color composite (R, 2.5; G, 1.5; B, 1.1 μm). (b) Parameter map color composite (R, D2400FRT (2% linear stretch 0.010–0.015); G, D2300FRT (2% linear stretch 0.003–0.008); B, D1900FRT (2% linear stretch 0.012–0.020)) (Table 2). Blue areas exhibit high D1900FRT parameter values consistent with the presence of hydrated materials, and magenta areas exhibit high D1900FRT and D2400FRT parameter values indicative of polyhydrated sulfates.

4.5.1. Hydrated Sulfate Exposures Located to the North, Northwest, and Northeast of LHS Deposits

[53] Polyhydrated sulfates detected ~20 km to the northwest of LHS deposits occur in a topographic low that is an extension of the northwest-southeast trending valley that contains LHS deposits (Figure 24, red pixels indicated with the black arrow). These polyhydrated sulfates occur at a similar elevation and in a similar setting to the LHS deposits, e.g., near the base of a heavily eroded section in which layers of $ET1_A$, $ET1_B$, and $ET1_C$ are exposed.

[54] Monohydrated and polyhydrated sulfates are detected near the base of $[ET1/LHS/LHS_{cap}]_{mantled}$ located ~40 km to the northeast of the LHS deposits in CRISM image FRT000099C8 (Figure 8) and FRT0000893E (Figure 25). These exposures occur at a similar elevation to upper layers of the LHS deposits. Exposures closest to the base of $[ET1/LHS/LHS_{cap}]_{mantled}$ are mantled with low-albedo fines and/or high-albedo dust. The stratigraphic relationships of the hydrated sulfate-bearing materials is difficult to determine because the hydrated sulfate exposures are limited in spatial extent and partially obscured by aeolian deposits. The hydrated sulfates either underlie or embay the higher-standing mesas of $[ET1/LHS/LHS_{cap}]_{mantled}$ and ET1. Spectra extracted from the hydrated sulfate bearing materials have relatively weak absorption features, consistent with contamination from mobile fines (Figure 26, FRT000099C8 poly and FRT0000893E poly). A restricted exposure of material with a monohydrated sulfate spectral signature (Figure 26, FRT000099C8 mono) also occurs ~5 km from the base of $[ET1/LHS/LHS_{cap}]_{mantled}$ in FRT000099C8 (Figure 8, green arrow).

[55] Both monohydrated and polyhydrated spectral signatures were also detected in CRISM image FRT000062E6 in materials that occur near the base of an outlier of ET1 located ~130 km to the north of LHS deposit (Figure 27). This outlier of ET1 is partially eroded and multiple mesas of ET1 occur in which $ET1_A$, $ET1_B$, and $ET1_C$ are exposed (Figure 6). Analysis of FRT000062E6 shows that hydrated spectral signatures are restricted to materials that occur at the base of the mesas of ET1 and are not detected in mesa walls (Figure 27; spectrum shown in Figure 26, FRT000062E6 poly). This indicates that the hydrated sulfate-bearing materials were deposited subsequent to the erosion of the ET1 mesas.

4.5.2. Hydrated Sulfate Exposures Located to the South, Southwest, and East of LHS Deposits

[56] Small exposures of polyhydrated sulfates were detected to the southwest of the valley in CRISM image FRT000097F8 and are limited to a cluster of pixels located near the center of the image (Figure 12; spectrum shown in Figure 26, FRT000097F8 poly). The material that exhibits a polyhydrated sulfate spectral signature occurs in the midst of a surface dominated by $ET1_B$ that was exposed following erosion of overlying $ET1_C$. The limited spatial extent of the polyhydrated sulfate exposures in FRT000097F8 makes stratigraphic analyses difficult. These polyhydrated sulfates were deposited either prior to the formation of $ET1_C$ or after the formation and subsequent erosion of $ET1_C$.

[57] Material with a polyhydrated sulfate spectral signature is exposed near the base of Ph in CRISM image FRT00003CE0 (Figure 28; spectrum shown in Figure 26, FRT00003CE0 poly) and in FRT0001252F (Figure 14c, magenta pixels indicated with a black arrow). The northwestern portion of FRT00003CE0 is partially mantled by aeolian debris. Polyhydrated sulfate spectral signatures are detected in areas that are relatively free from debris. Clean

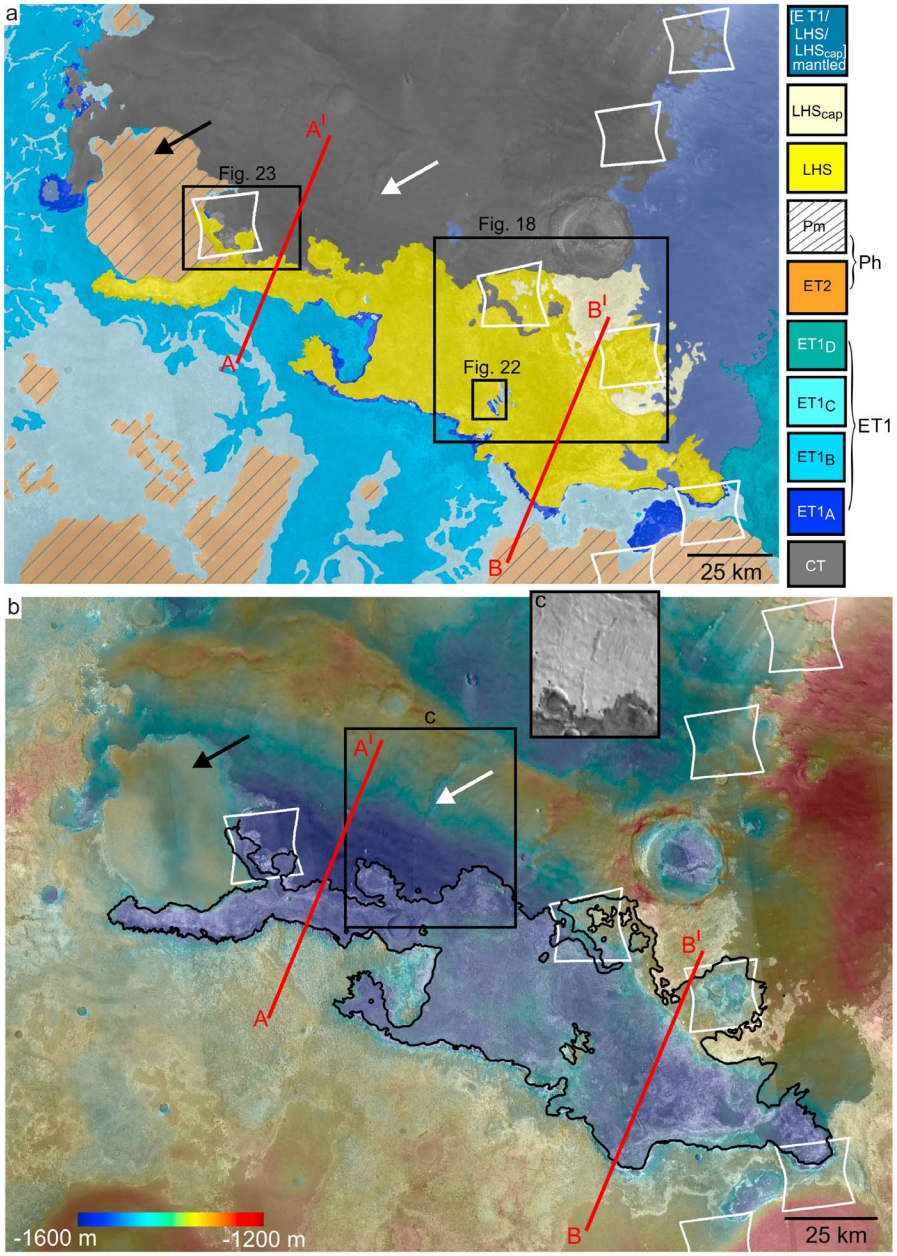

Figure 17. (a) Subset of the units map (Figure 4b) showing the extent of LHS deposits; location indicated in Figure 4a. The white arrow indicates the location of a channel feature that cuts a ridge in CT and is embayed by LHS deposits and the black arrow indicates a plateau capped by Ph. Red lines indicate locations of cross sections shown in Figure 29. (b) CTX mosaic with MOLA color-coded topography overlain. The extent of LHS deposits is outlined in black. LHS deposits associated with the northeast-southwest trending valley occur in both low- and high-elevation exposures. (c) THEMIS DIR mosaic covering the area outlined with the white box showing a channel feature that cuts a ridge in CT and is embayed by LHS deposits.

exposures of $ET1_C$ located in the northeastern portion of FRT00003CE0 are spectrally similar to the $ET1_C$ spectrum extracted from FRT000097F8 and exhibit spectral absorptions features at ~1.92 and 2.30 to 2.31 μm, consistent with the presence of Fe/Mg smectites (Figure 7, FRT00003CE0 $ET1_C$). The polyhydrated sulfate exposures in FRT00003CE0 overlie $ET1_C$ and either underlie or embay Ph. Polyhydrated sulfates detected in FRT0001252F are spectrally similar to those in FRT00003CEO and also occur in indurated material that overlies $ET1_C$ (Figure 14c).

[58] Polyhydrated sulfates are exposed in FRT0000CC22 near the margin of low-albedo mantle that covers a small area of $ET1_D$ located to the east of the LHS deposits (Figure 16b, magenta pixels). The polyhydrated sulfates overlie $ET1_D$

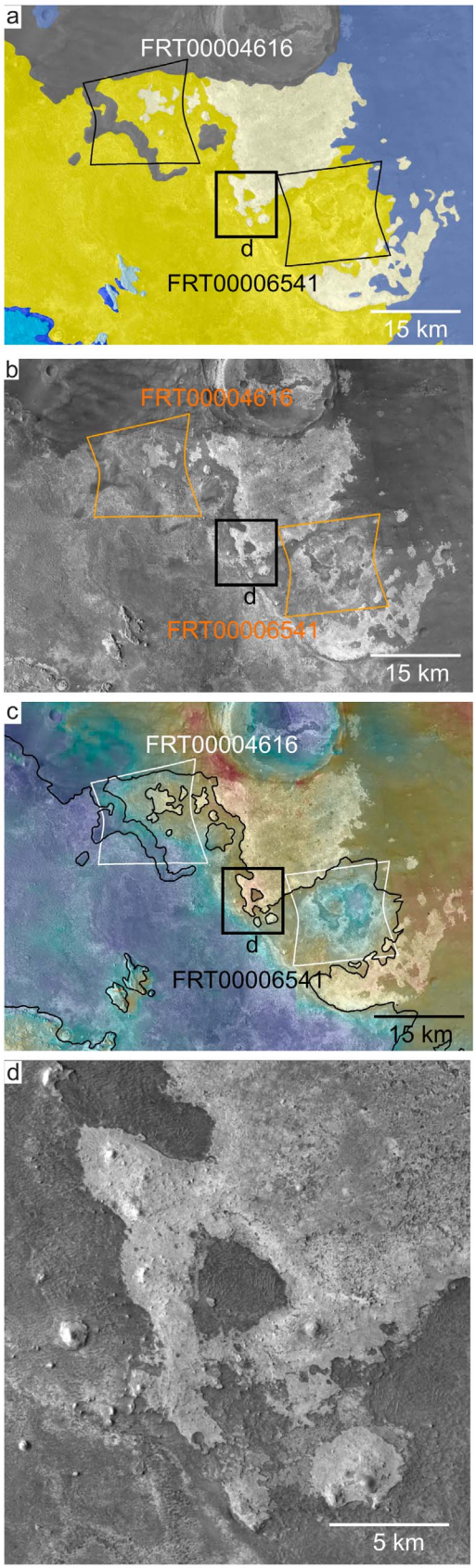

and are possibly remnants of a more extensive layer that was stripped by aeolian erosion in areas unprotected by the dark mantle.

5. Discussion

5.1. Stratigraphic Relationships, Northern Sinus Meridiani

[59] Three regionally extensive units, Cratered Terrain (CT); Etched Terrain 1 (ET1); and Plains, Hematite-bearing (Ph), are exposed in Sinus Meridiani (Figure 1, unit descriptions summarized in Table 1). ET1 is an indurated sedimentary unit that unconformably overlies CT and Ph occurs at the top of the regional stratigraphic section. Ph is a composite unit that consists of sedimentary rock, Etched Terrain 2 (ET2), that is overlain by an unconsolidated veneer, the Plains Mantle, Hematite-bearing (Pm) (Figure 4b).

[60] Detailed stratigraphic analyses presented in section 4 focused on an area in northern Sinus Meridiani located between 1°N to 5°N latitude and 3°W to 1°E longitude. Layered deposits associated with the ~120 km long northwest-southeast trending valley located in the center of the study area that exhibit hydrated sulfate spectral signatures were distinguished from ET1 and mapped as Layered Hydrated Sulfate (LHS) deposits. Upper layers associated with the LHS deposits that do not exhibit specific hydrated sulfate signatures were mapped as the Layered Hydrated Sulfate Cap (LHS_{cap}) (Figure 4b and Table 1). LHS deposits are exposed on the valley floor and within higher-elevation plateaus near the northeastern margin of the valley (Figures 17 and 18). ET1 was subdivided into four laterally continuous, stratigraphically distinct subunits, $ET1_A$, $ET1_B$, $ET1_C$, and $ET1_D$, that were mapped using superposition relationships (Figure 4b and Table 1). $ET1_A$ is the stratigraphically lowest subunit and $ET1_D$ is the stratigraphically highest. $ET1_A$ is spectrally bland between ~1.0 and 2.5 μm, $ET1_B$ exhibits a weak hydration feature at 1.9 μm, $ET1_C$ exhibits a Fe/Mg smectite spectral signature in some areas, and $ET1_D$ exhibits a strong hydration feature at 1.9 μm. The thickness of $ET1_A$ is variable (~150 m thick in places) and appears to be controlled by the underlying topography of CT. $ET1_B$ is 10 to 30 m thick, $ET1_C$ is a 40 to 60 m thick, and $ET1_D$ is composed of multiple strata that have a combined thickness of ~70 m where exposed in the study area.

5.1.1. Stratigraphic Relationships Between LHS Deposits and $ET1_A$, ETI_B, and $ET1_C$

[61] We constructed two vertical cross sections from MOLA elevation profiles that transect the LHS deposits (Figure 29, locations shown in Figure 17). Both cross sections are oriented roughly parallel to regional strike, in the northeast-southwest direction. LHS deposits that are exposed within plateaus near the northeastern margin of the valley

Figure 18. (a) Subset of the units map in Figure 17a showing high-elevation exposures of LHS deposits. (b) CTX mosaic. (c) CTX mosaic with MOLA color-coded topography overlain. (d) Higher-resolution view (subset of CTX image P03_002113_1825) showing mesas of LHS_{cap} that occur as outliers from larger exposures.

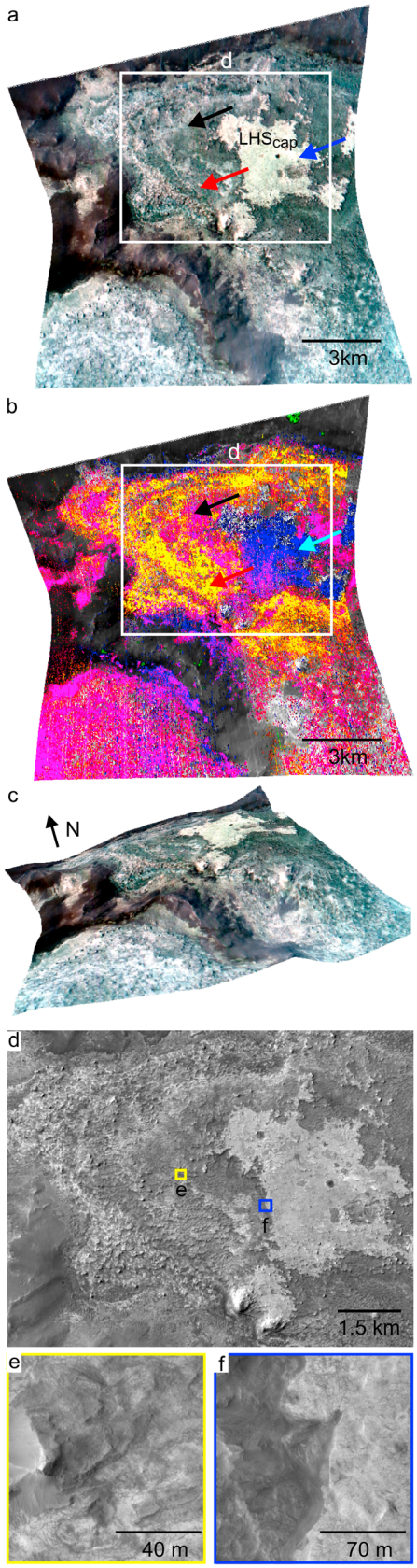

occur at significantly higher elevations than LHS deposits on the valley floor. These northeastern LHS deposits reach elevations that are similar in height to high-standing portions of ET1 located to the south of the valley (Figure 17). LHS deposits along the northeastern margin of the valley do not project to corresponding layers to the southwest of the valley (Figure 29b). We infer a lateral facies change to explain the observed configuration of the LHS deposits and ET1 because we found no evidence for post depositional structural deformation of the LHS deposits. Both conformable and unconformable facies changes are considered.

[62] If the LHS deposits are conformable with ET1 then a lateral facies change occurred in response to lateral variations in local depositional conditions that resulted in an abrupt contact with ET1 along the southern margin of the valley. If the LHS deposits are unconformable with ET1 then this implies that ET1 was originally laterally continuous and subsequently eroded and that LHS deposits embay ET1.

[63] On the basis of detailed analysis presented in section 4, we favor an unconformable facies change in which $ET1_A$, $ET1_B$, and $ET1_C$ (and likely ET2, see discussion in section 5.2) were originally laterally continuous, subsequently eroded, and embayed by younger LHS deposits. The presence of outliers of ET1 located in the northern portion of the study area in which layers of $ET1_A$, $ET1_B$, and $ET1_C$ are exposed, the same sequence of strata observed in large expanses of ET1 located to the south and west of the LHS deposits, supports the hypothesis that $ET1_A$, $ET1_B$, and $ET1_C$ were originally laterally extensive across the study area

Figure 19. CRISM image FRT00004616 (footprint shown in Figure 18) showing CT, LHS deposits, and LHS_{cap}. LHS deposits embay CT. The black, red, and blue arrows indicate locations of spectra shown in Figure 21 labeled as FRT00004616 LHS poly, FRT00004616 LHS mono, and FRT00004616 LHS_{cap}, respectively. (a) False color composite (R, 2.5; G, 1.5; B, 1.1 μm). (b) Parameter map color composite (R, D2400FRT (2% linear stretch 0.015–0.025); G, D2100FRT (2% linear stretch 0.015–0.025), B, D1900FRT (2% linear stretch 0.015–0.025)) (Table 2) with the D2300FRT index overlain in green, overlain on a 1.1 μm gray scale image. Blue areas exhibit high D1900FRT parameter values consistent with the presence of hydrated materials, magenta areas exhibit high D1900FRT and D2400FRT parameter values indicative of polyhydrated sulfates, yellow areas exhibit high D2100FRT and D2400FRT parameter values indicative of monohydrated sulfates, and green areas exhibit high D2300FRT parameter values indicative of Fe/Mg phyllosilicates. High D2300FRT parameter values occur in small areas of CT, consistent with Fe/Mg smectites detected in FRT000099C8 (Figure 8). (c) CRISM FRT00004616 draped on MOLA topography (vertical exaggeration is 10). (d) Light- and dark-toned layers are evident in LHS deposits (subset of CTX image T01_000886_1819). (e) Both light- and dark-toned materials are indurated (subset of HiRISE image PSP_002680_1825). (f) Subset of HiRISE image PSP_002680_1825 showing the contact between LHS deposits and LHS_{cap}.

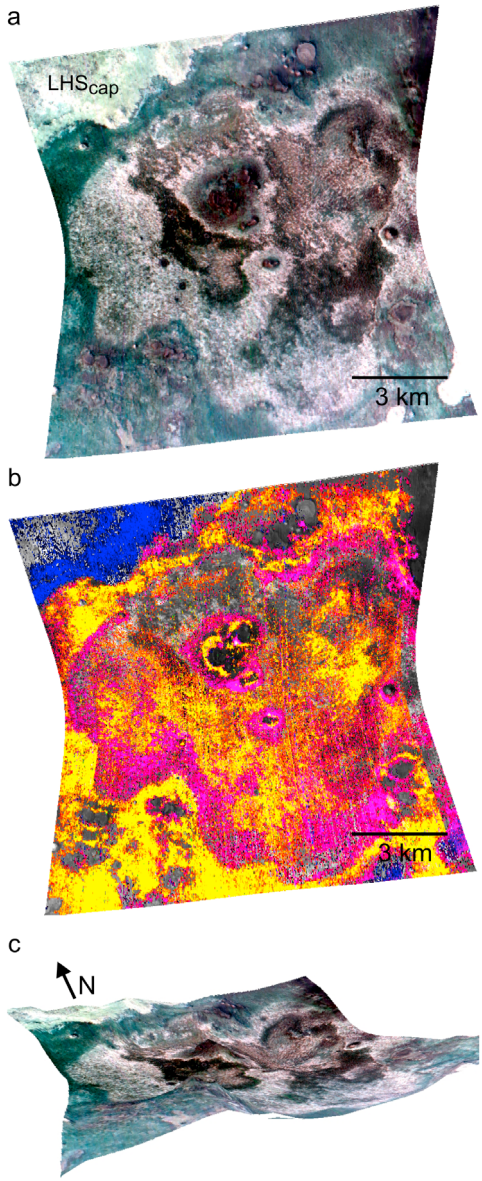

Figure 20. CRISM image FRT00006541 (footprint shown in Figure 18) showing LHS deposits and LHS_{cap}. (a) False color composite (R, 2.5; G, 1.5; B, 1.1 μm). (b) Parameter map color composite (R, D2400FRT (2% linear stretch 0.015–0.025); G, D2100FRT (2% linear stretch 0.015–0.025); B, D1900FRT (2% linear stretch 0.015–0.025)) (Table 2) overlain on a 1.1 μm gray scale image. Blue areas exhibit high D1900FRT parameter values consistent with the presence of hydrated materials, magenta areas exhibit high D1900FRT and D2400FRT parameter values consistent with the presence of polyhydrated sulfates, and yellow areas exhibit high D2100FRT and D2400FRT parameter values consistent with the presence of monohydrated sulfates. (c) CRISM image FRT00006541 draped on MOLA topography (vertical exaggeration is 10).

(Figure 4b). The occurrence of exposures of $ET1_A$ in both the scarp wall along the southern margin of the LHS deposits (Figure 14) and on the northwestern valley floor underlying LHS deposits (Figure 23c) is consistent with an unconformable facies change because $ET1_A$ is observed to be a thick, relatively easily erodible unit. The presence of isolated mesas located in the center of the valley that exhibit the same sequence of layers ($ET1_A$, $ET1_B$, and $ET1_C$) observed in the scarp wall along the southern margin of the valley that appear to be embayed by LHS deposits (Figure 22) is consistent with an unconformable facies change and inconsistent with a conformable facies change.

5.1.2. Stratigraphic Relationships Between $ET1_C$, $ET1_D$, and ET2

[64] $ET1_D$ occurs stratigraphically above $ET1_C$ and appears to underlie ET2 in the eastern portion of the study area (Figures 4c, vertical section A1, and 15). However, the possibility that $ET1_D$ postdates and therefore embays ET2 cannot be excluded (Figure 4c, vertical section A2). $ET1_D$ is not identified in the western and southwestern portion of the study area (Figure 4b). The units map shown in Figure 4b in which $ET1_D$ is exposed only in the eastern portion of the study area could be produced by two possible vertical configurations: configuration 1, where $ET1_D$ occurs between $ET1_C$ and ET2 in the eastern and western portion of the

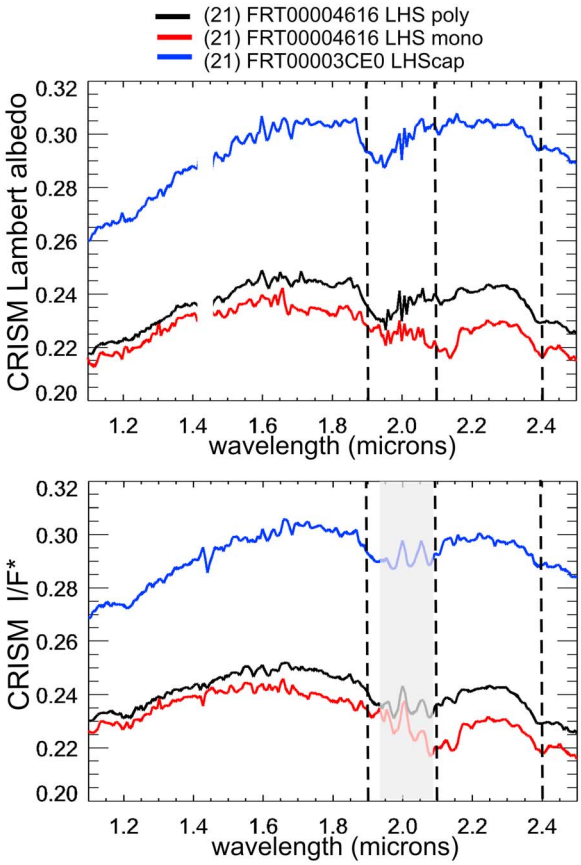

Figure 21. (top) Lambert albedo spectra retrieved using DISORT modeling extracted from areas indicated with arrows in Figure 19. (bottom) CRISM *I*/*F** (volcano scan and cos(*i*) corrected CRISM *I*/*F*) spectra for areas shown in the top plot. Residual atmospheric features are likely to occur in the region of the spectrum highlighted in gray in which intense atmospheric CO_2 absorptions occur. Each spectrum is the average of 25 spectra.

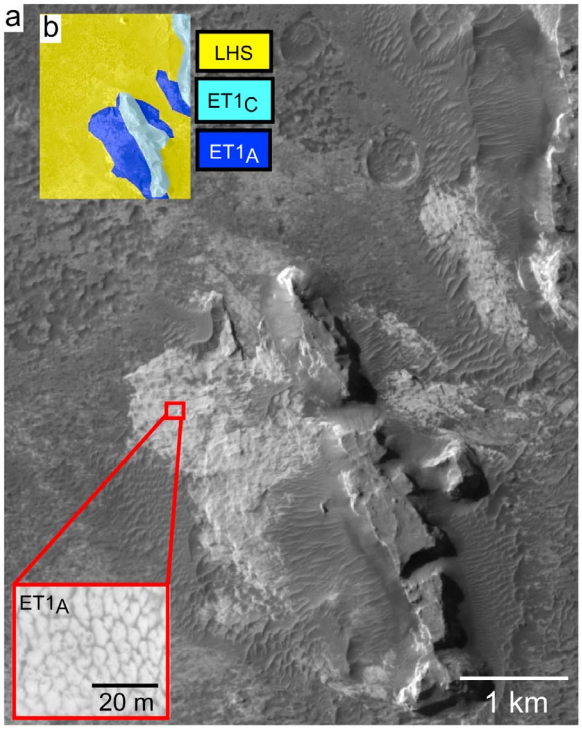

Figure 22. (a) Mesas within the valley (location shown in Figure 17) that exhibit the same sequence of layers ($ET1_A$, $ET1_B$, $ET1_C$) that occur in the scarp wall along the southern margin of the valley appear to be embayed by LHS deposits (subset of CTX image T01_000886_1819). The red inset shows the scalloped morphology of $ET1_A$ (subset of HiRISE image PSP_006148_1820). (b) Units map of area shown in Figure 22a.

study area but was eroded back where not protected by overlying ET2 such that the margin of $ET1_D$ is approximately coincident with the margin of ET2 in western locations, making $ET1_D$ difficult to identify (Figure 4c, vertical section B1) or configuration 2, where ET2 occurs directly stratigraphically above $ET1_C$ in the western portion of the study area (Figure 4c, vertical section B2).

[65] Both configurations 1 and 2 could be produced by depositional settings in which $ET1_D$ was originally laterally continuous. If $ET1_D$ was originally laterally continuous, then either $ET1_D$ was buried by ET2 and subsequently eroded in the western portion of the study area, resulting in configuration 1, or $ET1_D$ was eroded prior to the unconformable deposition of ET2, resulting in configuration 2. However, if deposition and/or diagenesis of $ET1_D$ were laterally variable, then configuration 1 would be observed if $ET1_D$ was originally laterally continuous but the western portion of $ET1_D$ was pervasively altered during diagenesis to form lower strata of ET2 and configuration 2 would have resulted if deposition of $ET1_D$ was restricted to eastern locations. Alternatively, configuration 2 would result if $ET1_D$ postdated ET2 formation and embays ET2 (Figure 4c, vertical section A2). Discrimination between configuration 1 and configuration 2 to explain the lack of exposure of $ET1_D$ in the western portion of the study area is difficult because multiple mechanisms can plausibly produce both config-

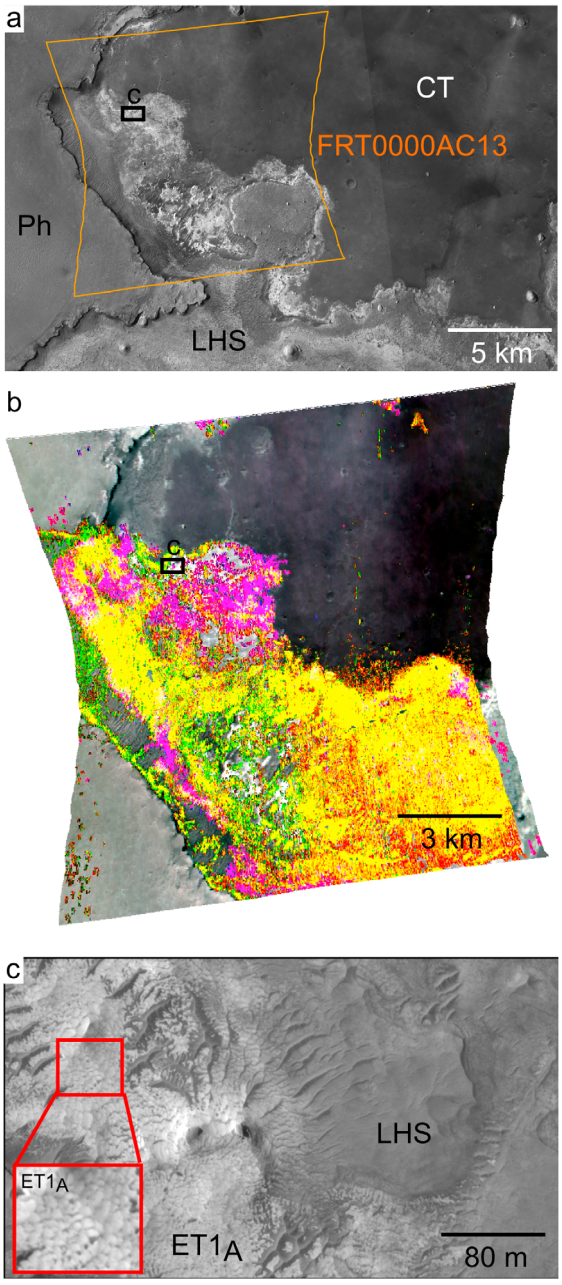

Figure 23. (a) CTX mosaic subset showing the contact between CT and LHS deposits; location shown in Figure 17. (b) False color composite of CRISM image FRT0000AC13 (R, 2.5; G, 1.5; B, 1.1 μm) with parameter map color composite overlain (R, D2400FRT (2% linear stretch 0.015–0.025); G, D2100FRT (2% linear stretch 0.015–0.025), B, D1900FRT (2% linear stretch 0.015–0.025)) (Table 2). Blue areas exhibit high D1900FRT parameter values consistent with the presence of hydrated materials, magenta areas exhibit high D1900FRT and D2400FRT parameter values indicative of polyhydrated sulfates, and yellow areas exhibit high D2100FRT and D2400FRT parameter values indicative of monohydrated sulfates. (c) LHS deposits with an intermediate albedo overlie light-toned $ET1_A$ (subset of HiRISE image PSP_001691_1825). The red inset shows the distinctive scalloped morphology of $ET1_A$.

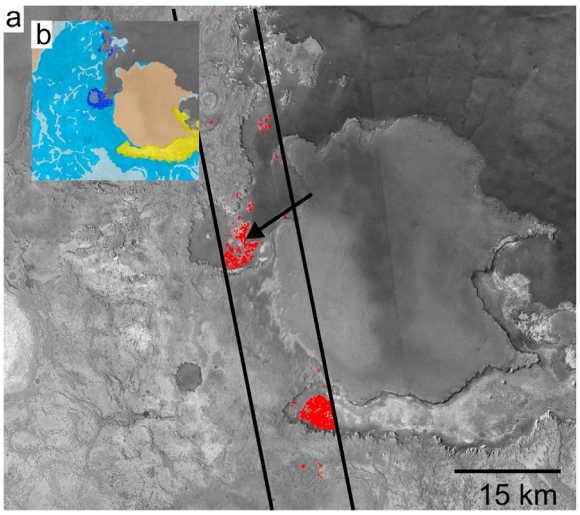

Figure 24. (a) Subset of the CTX mosaic shown in Figure 4a with the footprint of CRISM MSW00005AD3 outlined in black. Red pixels exhibit high D1900 and D2400 parameter values (Table 2), consistent with the presence of polyhydrated sulfates. The black arrow indicates the location of hydrated sulfates detected to the northwest of LHS deposits. (b) Units map of area shown in Figure 24a; map key is shown in Figure 17a.

urations and $ET1_D$ and ET2 only contact for a short interval in the eastern portion of the study area (Figure 15).

5.2. Relative Age Relationships Between LHS Deposits, ET1, and ET2

[66] The occurrence of mesas formed from $ET1_A$, $ET1_B$, and $ET1_C$ located in the valley that are embayed by LHS deposits (Figure 22) requires that the LHS deposits postdate the formation of $ET1_A$, $ET1_B$, and $ET1_C$. Therefore, LHS deposits embay $ET1_A$ (Figure 29) where they contact for ~120 km along the southern margin of the valley (Figure 17).

[67] Ph occurs on the surface of a plateau that forms the western margin of the valley (Figure 17, black arrow) and on high-standing surfaces to the south of the valley. LHS deposits contact with $ET1_A$ at the base of the plateau along their western margin (Figure 17). The presence of Ph on these high-standing surface and the lack of Ph in the valley suggests that ET2 (the bedrock component of Ph) formed prior to the erosion of ET1 and subsequent deposition of the LHS deposits. This indicates that LHS deposits and LHS_{cap} may be the youngest stratigraphic units exposed in northern Sinus Meridiani and that LHS deposits postdate the formation of ET2.

[68] $ET1_D$ occurs stratigraphically above $ET1_C$ and appears to underlie ET2. However, the inference that $ET1_D$ predates ET2 is not definitive and it is possible that $ET1_D$ is younger than ET2. Materials mapped as LHS_{cap} and $ET1_D$ are geomorphically and spectrally similar but are separated by surfaces covered by low-albedo mantle deposits that preclude determination of the stratigraphic relationship between LHS_{cap} and $ET1_D$ (Figure 15). It is possible that $ET1_D$ is laterally continuous with LHS_{cap} (Figure 4d). If so, this is not inconsistent with a relatively young age for LHS and LHS_{cap}, but may indicate that LHS deposits predate the formation of ET2. However, if LHS deposits predate the formation of ET2, it is difficult to explain the presence of

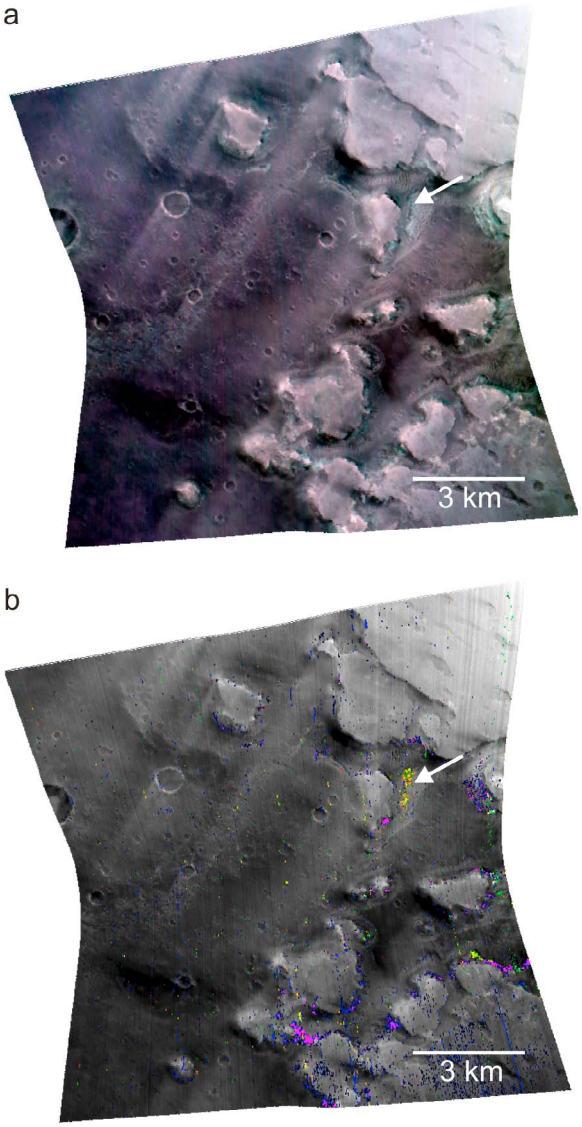

Figure 25. CRISM image FRT0000893E (footprint shown in Figures 4 and 9) showing the contact between CT and $[ET1/LHS/LHS_{cap}]_{mantled}$. The white arrow indicates the location of a spectrum extracted from FRT0000893E shown in Figure 26 (FRT0000893E mono). (a) False color composite (R, 2 0.5; G, 1.5; B, 1.1 μm). (b) Parameter map color composite (R, D2400FRT (2% linear stretch 0.010–0.015); G, D2100FRT (2% linear stretch 0.015–0.025); B, D1900FRT (2% linear stretch 0.012–0.022)) (Table 2) overlain on a 1.1 μm gray scale image. Blue areas exhibit high D1900FRT parameter values consistent with the presence of hydrated materials, magenta areas exhibit high D1900FRT and D2400FRT parameter values indicative of polyhydrated sulfates, and yellow areas exhibit high D2100FRT and D2400FRT parameter values indicative of monohydrated sulfates. Hydrated sulfate detections occur near the base of the plateau of $[ET1/LHS/LHS_{cap}]_{mantled}$.

ET2 on plateau surfaces whose walls are embayed by LHS deposits.

5.3. LHS Deposits

5.3.1. Original Thickness and Extent of LHS Deposits

[69] The current exposures of LHS deposits represent a lower bound to the original extent of these deposits. There is morphologic evidence for differential erosion of the LHS deposits that includes the presence of plateaus and small-scale pits and groves (Figures 18 and 19d). LHS deposits are ~50 m thick near their northwestern margin and ~150 m thick near their northeastern margin (Figures 17 and 18). LHS deposits extend to the scarp walls along the western, southern, and eastern margins of the valley. However, LHS deposits terminate in low mesas along their northwestern margin. This indicates that the LHS deposits may have originally extended further to the north (Figure 23). The occurrence of hydrated sulfate-bearing materials ~30 km to the northwest of the LHS deposits (Figure 24) in a stratigraphically similar setting as the LHS deposits provides additional evidence that the LHS deposits may have extended further to the north. Additional hydrated sulfate-bearing materials that were detected to the north, northeast, south, southwest, and east of the LHS deposits are discussed in section 5.4.

5.3.2. Candidate Formation Environments

[70] LHS deposits are exposed both on the valley floor and within higher-elevation plateaus near the northeastern margin of the valley (Figure 17). Exposures directly to the northeast of the higher-standing portion of the LHS deposits and LHS_{cap} are mantled by dark material that obscures identification of underlying units and potential contacts between these units. Emplacement of the LHS deposits was shown via embayment and crosscutting relationships to postdate CT, which rises to form a ridge to the north of the LHS deposits (Figure 17b). LHS deposits were also shown to postdate the formation of the scarp wall in ET1 that forms the eastern, southern, and southwestern margins of the valley (Figure 17). Therefore, prior to the formation of LHS deposits, the topographic configuration of materials surrounding the valley resulted in the presence of a nearly closed basin. The occurrence of a thick sequence of layered deposits with hydrated sulfate spectral signatures within this nearly closed valley is suggestive of deposition in an evaporitic setting.

[71] The observed compositional layering in the LHS deposits, specifically intercalated layers of monohydrated and polyhydrated sulfates (Figures 19 and 20), implies that multiple wetting events, brine recharge, or fluctuations in evaporation rate occurred to produce depositional layering, although diagenetic processes may have modified the initial layering. Differences in albedo between layers in the LHS deposits could have resulted at least partially from variable contributions of siliciclastic components, including low-albedo basaltic fines and high-albedo dust.

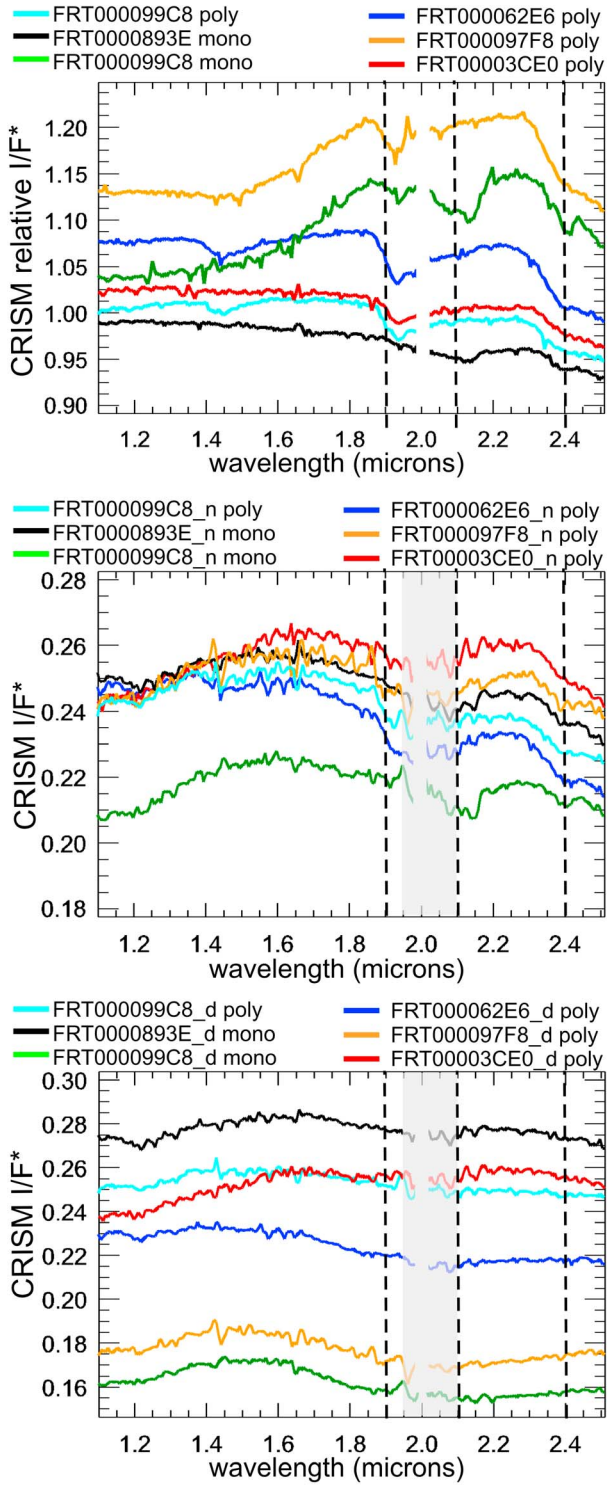

Figure 26. (top) CRISM relative reflectance spectra extracted from areas of selected FRTs with hydrated sulfate-like spectral signatures. (middle) CRISM *I*/*F** (volcano scan and cos(*i*) corrected CRISM *I*/*F*) numerator (_n) spectra that were used to generate the ratio spectra shown in the top plot. (bottom) CRISM *I*/*F** (volcano scan and cos(*i*) corrected CRISM *I*/*F*) denominator (_d) spectra that were used to generate the ratio spectra shown in the top plot. Residual atmospheric features are likely to occur in the region of the spectrum highlighted in gray in which intense atmospheric CO_2 absorptions occur. Each spectrum is the average of 25 spectra.

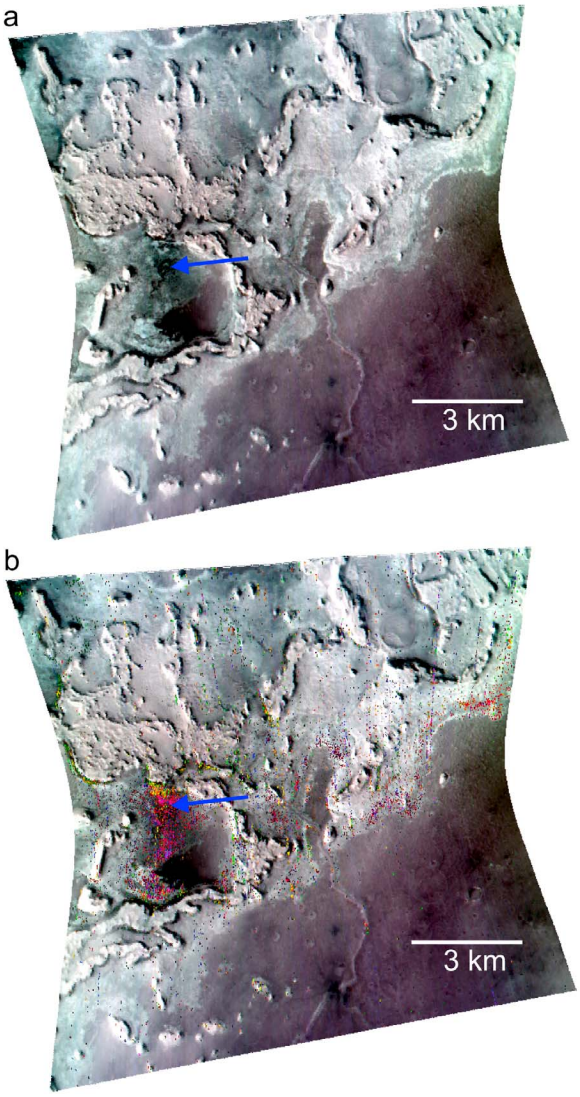

Figure 27. CRISM image FRT000062E6 (footprint shown in Figures 4 and 6) showing eroded mesas of ET1 that overlie CT. The blue arrow indicates the location of a spectrum extracted from FRT000062E6 shown in Figure 26 (FRT000062E6 poly). (a) False color composite (R, 2.5; G, 1.5; B, 1.1 μm). (b) Parameter map color composite (R, D2400FRT (2% linear stretch 0.012–0.022); G, D2100FRT (2% linear stretch 0.015–0.025); B, D1900FRT (2% linear stretch 0.012–0.022)) (Table 2) overlain on Figure 27a. Magenta areas exhibit high D1900FRT and D2400FRT indicative of polyhydrated sulfates, and yellow areas exhibit high D2100FRT and D2400FRT parameter values indicative of monohydrated sulfates. Hydrated sulfate detections occur near the base of mesas of ET1.

[72] The exact depositional setting in which the LHS deposits formed is uncertain. LHS exposures could be consistent with formation in deep or shallow saline aquifers, surface brines, or some combination of these. The presence of LHS deposits at relatively high elevations along the northeastern margin of the valley implies that brines reached this level. These high-elevation layers could be consistent with deposition in a deep water basin setting in which a thicker evaporitic sequence is deposited along shallow margins of the basin and a thinner sequence of evaporitic deposits accumulates in the deeper central portion of the basin [e.g., *Hovorka et al.*, 2007]. The asymmetry of the valley basin, specifically the relatively steep southern margin and the gentle rise to the north of the LHS deposits (Figure 29a) may have resulted in accumulation of significant evaporitic deposits along the northern margin only. In this scenario, a sequence of LHS deposits similar to those that occur in the northeastern portion of the valley should have also formed along the northwestern margin. However, a thick sequence of LHS deposits is not observed in this area. It is possible that additional layers were deposited to the northwest and subsequently eroded. There is some evidence that the LHS deposits originally extended further to the north (section 5.3.1). Alternatively, the valley may have been episodically inundated with shallow brines that evap-

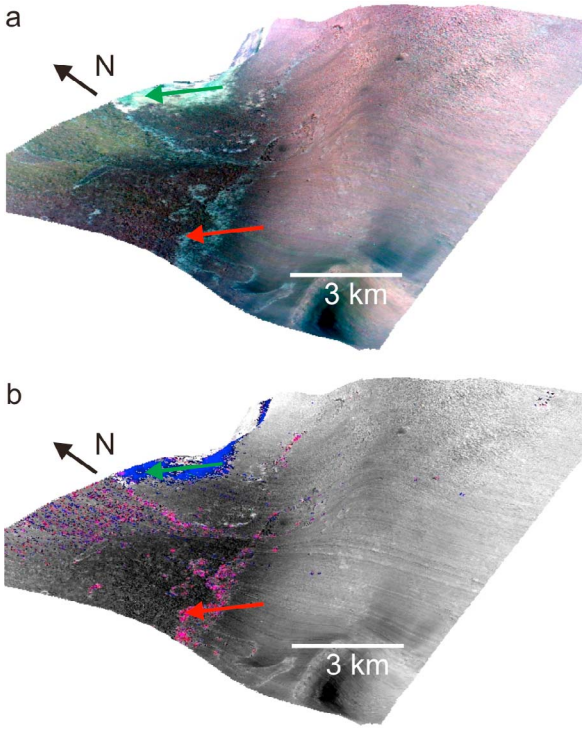

Figure 28. CRISM image FRT00003CE0 (footprint shown in Figure 4) draped on MOLA topography (vertical exaggeration is 10). Ph is exposed in the northeastern portion of the image. The green and red arrows indicate locations of spectra extracted from FRT00003CE0 shown in Figure 7 (FRT00003CE0 $ET1_C$) and Figure 26 (FRT00003CE0), respectively. (a) False color composite (R, 2.5; G, 1.5; B, 1.1 μm). (b) Parameter color composite (R, D2400FRT (2% linear stretch 0.012–0.022); G, D2300FRT (2% linear stretch 0.003–0.008), B, D1900FRT (2% linear stretch 0.015–0.025)) (Table 2). Blue areas exhibit high D1900FRT parameter values consistent with the presence of hydrated materials, magenta areas exhibit high D1900FRT and D2400FRT parameter values indicative of polyhydrated sulfates, and green areas exhibit high D2300FRT parameter values indicative of Fe/Mg phyllosilicates.

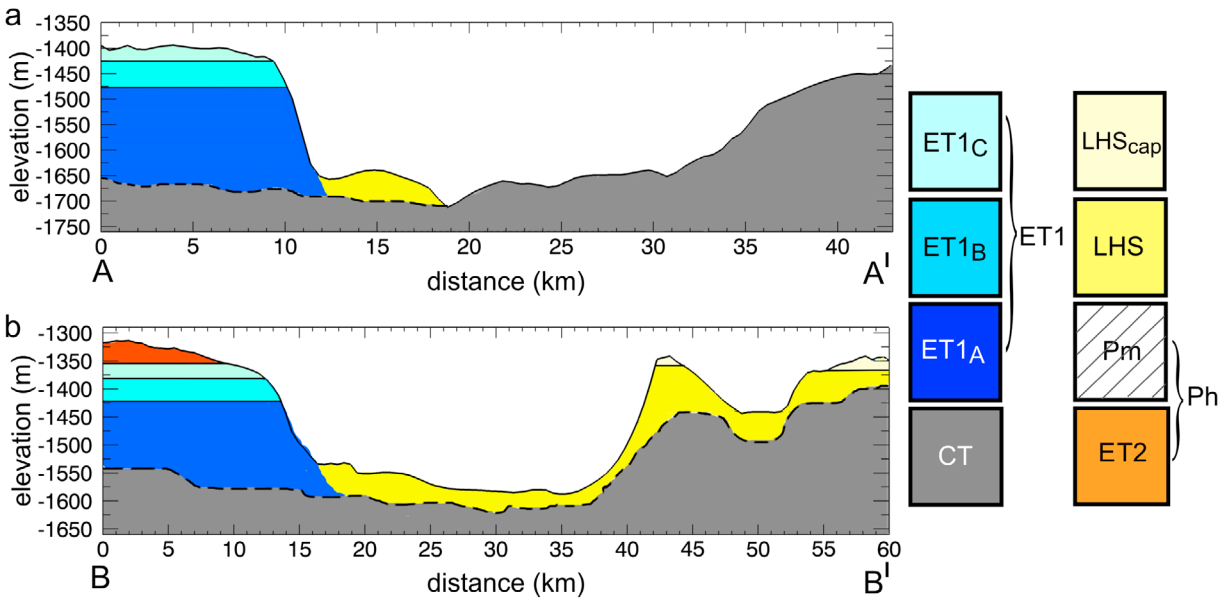

Figure 29. Cross sections generated from MOLA topographic profiles along the red lines indicated in Figure 17 from (a) A to A′ and (b) B to B′. Profiles are oriented roughly along the direction of regional strike. The inferred stratigraphy for each cross section is shown (units are the same as those mapped in Figures 4b and 17a). LHS deposits appear to embay $ET1_A$.

orated to leave layers cemented with hydrated sulfates that accumulated on the valley floor and near the northeastern margin, incrementally shallowing the basin or portions of the basin. In this scenario, it is possible, but not required, that the valley eventually filled with LHS deposits and the northeastern layers are late-stage deposits. If this were the case, then subsequent erosion stripped substantial amounts of material from the valley resulting in the current configuration of the LHS deposits.

5.4. Implications of Additional Hydrated Sulfate Exposures

[73] Exposures with hydrated sulfate spectral signatures are not restricted to LHS deposits. Multiple spatially limited hydrated sulfate exposures were detected in the study area in northern Sinus Meridiani, some of which are only evident in the highest spatial resolution CRISM images (20 m/pixel). Hydrated sulfates were identified on both relatively low- and high-standing surfaces. Some of these hydrated sulfate exposures occur in topographic shadows or near the margins of mantled areas and appear to be erosional remnants of deposits that were originally more extensive.

[74] Hydrated sulfates were detected in three locations within low areas located 30 km to the northwest, 40 km to the northeast, and 130 km to the north of the LHS deposits, respectively (section 4.5.1). These northern exposures of hydrated sulfates occur at similar elevations to upper layers of the LHS deposits and are consistent with deposition following substantial differential erosion of $ET1_A$, $ET1_B$, and $ET1_C$. It is possible that these northern exposures of hydrated sulfates are genetically related to the LHS deposits or formed during the same time period by similar processes but in different local environments.

[75] Hydrated sulfates were also detected in limited locations on high-standing surfaces of ET1 located to the southwest, south, and east of the LHS deposits (section 4.5.2). Although the relatively small spatial extent and/or poor quality of these exposures hinder stratigraphic analyses, these hydrated sulfates are constrained to postdate $ET1_B$ formation. One hydrated sulfate-bearing exposure overlies $ET1_C$ and may occur in lower layers of ET2 (the bedrock component of Ph) or $ET1_D$ and another exposure overlies $ET1_D$.

[76] The presence of multiple small exposures of hydrated sulfates separated by large expanses suggests that formation of deposits with hydrated sulfate spectral signatures was widespread. The stratigraphic context of these hydrated sulfate deposits is consistent with that of the LHS deposits and may record relatively late stage wetting events driven by groundwater.

5.5. Spectral and Textural Differences Between LHS Deposits and ET2

[77] Although the bedrock component of Ph, ET2, is known to be sulfate rich based on in situ MER Opportunity rover investigations, NIR spectra of this unit typically do not exhibit distinct vibrational features associated with hydrated and/or hydroxylated phases (Figure 7, FRT000097F8_d Ph) [*Arvidson et al.*, 2006]. In contrast, spectra extracted from LHS deposits in the valley exhibit relatively strong vibrational features indicative of the presence of both monohydrated and polyhydrated sulfates (Figure 21). Gray crystalline hematite was detected in orbital IR spectra of Ph but not of the LHS deposits [*Christensen et al.*, 2001b]. Analyses made by the Opportunity rover along its traverse revealed that ET2 is chemically homogenous [*Rieder et al.*, 2004]. In contrast, compositional layering that likely records

fluctuations in brine concentration or composition is observed in LHS deposits.

[78] The erosional texture of the LHS deposits is variable, but groves and pits are typically present at intermediate spatial scales (Figures 19c and 19d). In contrast, ET2 is relatively smooth at a similar spatial scale (Figure 11f). ET2 is extensively covered by a mantle (Pm) that armors the surface and slows deflation [*Sullivan et al.*, 2005]. Coatings on ET2 were identified in Opportunity rover observations [*Knoll et al.*, 2008]. Extensive coatings or alteration/dehydration rinds present at the surface of ET2 could obscure the spectral signature of underlying hydrated and/or hydroxylated sulfate minerals in orbital NIR reflectance spectra. In contrast, there is geomorphic evidence that LHS deposits are easily erodible. The time scale of erosion may be shorter than that of coating formation for the LHS deposits.

5.6. Scale of Evaporitic Setting and Comparison to Other Deposits on Mars

[79] The largest exposure of gray crystalline hematite detected on Mars occurs in Meridiani Planum [*Christensen et al.*, 2001b]. Smaller exposures of gray hematite were detected within Aram Chaos and in association with some interior layered deposits (ILDs) in Valles Marineris [*Christensen et al.*, 2001b]. Crater counts indicate that the Meridiani Planum hematite-bearing unit formed in the late Noachian to early Hesperian [*Arvidson et al.*, 2006], but that the Aram Chaos hematite-bearing deposits may have formed later in Martian history (or have been buried and exhumed), during the late Hesperian period [*Rotto and Tanaka*, 1995; *Glotch and Christensen*, 2005]. The Valles Marineris ILDs are also inferred to be Hesperian in age [*Scott and Tanaka*, 1986].

[80] Monohydrated sulfates and other hydrated minerals in Aram Chaos occur near exposures containing gray crystalline hematite [*Gendrin et al.*, 2005; *Glotch and Christensen*, 2005; *Noe Dobrea et al.*, 2008; *Lichtenberg et al.*, 2010]. Gray hematite deposits detected in Valles Marineris typically occur near the base of ILDs [*Christensen et al.*, 2001b] and both monohydrated and polyhydrated sulfates also occur in some ILDs [*Mangold et al.*, 2008; *Bishop et al.*, 2009; *Murchie et al.*, 2009b]. Hydrologic modeling predicts that groundwater upwelling occurred in Sinus Meridiani, Aram Chaos, and Valles Marineris during the late Noachian and the Hesperian [*Andrews-Hanna et al.*, 2007, 2010]. The observed hydrated sulfate and hematite-bearing deposits in these locations are consistent with formation in a groundwater driven evaporitic regime.

5.7. Fe/Mg Phyllosilicate-Bearing Deposits

5.7.1. Implications

[81] Fe/Mg smectites are detected in limited exposures associated with the oldest unit (CT) in the study area and on surfaces of $ET1_C$, a sedimentary unit that predates the formation of ET2, the sulfate and hematite-bearing unit explored by the Opportunity rover (Figure 4b). The presence of Fe/Mg smectites on the surface of $ET1_C$ indicates that this unit formed in a geochemical environment that differed from that of ET2, although it is also possible that the Fe/Mg smectites were transported to and preserved in $ET1_C$. The low pH conditions experienced by ET2 are probably not representative of the conditions that prevailed during the formation of ET1. The detection of phyllosilicate-bearing deposits in association with the oldest terrains in northern Sinus Meridiani is consistent with the hypothesis that phyllosilicates formed within the oldest terrains on Mars and that geochemical conditions became less favorable for phyllosilicate formation in later periods [*Poulet et al.*, 2005; *Bibring et al.*, 2006].

5.7.2. Spectral Comparisons

[82] The phyllosilicate-bearing deposits associated with CT are characterized spectrally by absorption features at 1.91 and 2.30 to 2.31 μm, consistent with the presence Fe/Mg smectites (Figures 2 and 7). The ~2.3 μm band is relatively deeper than the ~1.9 μm feature in these deposits and chlorite may also contribute to the spectral signature. A similar spectral shape occurs within Fe/Mg phyllosilicate-bearing deposits detected to the south within Miyamoto crater [*Wiseman et al.*, 2008]. Phyllosilicate-bearing deposits in $ET1_C$ exhibit shallow bands at 1.92 and 2.30 to 2.31 μm, consistent with the presence of Fe/Mg smectite (Figures 2 and 7). The ~1.9 μm feature is relatively stronger than the 2.31 μm band in spectra of $ET1_C$. Fe/Mg phyllosilicates exposed in ET1 to the east of our study area also exhibit a relatively strong ~1.9 μm feature [*Poulet et al.*, 2008].

[83] The fact that the phyllosilicate-bearing materials associated with $ET1_C$ have slightly different spectral shapes than older phyllosilicate-bearing deposits in Sinus Meridiani may be significant. However, several factors, including the composition [e.g., *Calvin and King*, 1997], the degree of crystallinity, the amount of hydration and/or absorbed water in a sample [*Milliken and Mustard*, 2005], or the presence of coatings [*Cooper and Mustard*, 1999], can contribute to the strength of the ~1.9 μm band. In addition, the abundance of the phyllosilicates influences band strengths and mixing with additional hydrated phases can affect the relative strength and apparent wavelength center of the 1.9 μm band.

6. Conclusion

[84] Sedimentary deposits indicative of an aqueous history that evolved over time are preserved in Sinus Meridiani. Laterally continuous strata were mapped over 100s of kilometers in extensive indurated sedimentary deposits (ET1) that predate the formation of the sulfate and hematite-bearing unit (Ph) explored by the MER rover Opportunity. A thick sequence (~150 m thick is some locations) of layered monohydrated and polyhydrated sulfate (LHS) deposits that are texturally and spectrally distinct from the sulfate- and hematite-bearing unit (Ph) explored by Opportunity were unconformably deposited following the extensive erosion of older sedimentary units ($ET1_A$, $ET1_B$, $ET1_C$). Therefore, at least two episodes of deposition separated by an unconformity occurred in northern Sinus Meridiani. These hydrated sulfate deposits may postdate the formation of Ph and, if so, record a relatively late-stage wetting event. The presence of Fe/Mg smectites in older sedimentary deposits ($ET1_C$) indicates that the low pH formation conditions inferred for the younger sulfate and hematite-bearing unit (Ph) are not representative of the aqueous geochemical environment that prevailed during the formation of earlier sedimentary materials (ET1) and alteration of the oldest terrains (CT) exposed in Sinus Meridiani.

[85] **Acknowledgments.** The authors acknowledge financial support from the NASA Mars Reconnaissance Orbiter project and the NASA Graduate Student Research Program and thank the CRISM, OMEGA, CTX, and HiRISE operations teams for their efforts.

References

Andrews-Hanna, J. C., R. J. Phillips, and M. T. Zuber (2007), Meridiani Planum and the global hydrology of Mars, *Nature*, *446*, 163–166, doi:10.1038/nature05594.

Andrews-Hanna, J. C., M. T. Zuber, and W. B. Banerdt (2008), The Borealis basin and the origin of the Martian dichotomy, *Nature*, *453*, 1212–1215, doi:10.1038/nature07011.

Andrews-Hanna, J. C., M. T. Zuber, R. E. Arvidson, and S. M. Wiseman (2010), Early Mars hydrology: 1. The Meridiani playa deposits and the sedimentary record of Arabia Terra, *J. Geophys. Res.*, *115*, E06002, doi:10.1029/2009JE003485.

Arvidson, R. E., F. P. Seelos IV, K. Deal, W. Koeppen, N. Snider, J. Kieniewicz, B. M. Hynek, M. Mellon, and J. Garvin (2003), Mantled and exhumed terrains in Terra Meridiani, Mars, *J. Geophys. Res.*, *108*(E12), 8073, doi:10.1029/2002JE001982.

Arvidson, R. E., F. Poulet, J.-P. Bibring, M. Wolff, A. Gendrin, R. V. Morris, J. J. Freeman, Y. Langevin, N. Mangold, and G. Bellucci (2005), Spectral reflectance and morphologic correlations in eastern Terra Meridiani, Mars, *Science*, *307*, 1591–1594, doi:10.1126/science.1109509.

Arvidson, R. E., et al. (2006), Nature and origin of the hematite-bearing plains of Terra Meridiani based on analysis of orbital and Mars Exploration Rover data sets, *J. Geophys. Res.*, *111*, E12S08, doi:10.1029/2006JE002728.

Barlow, N., J. Boyce, F. Costard, R. Craddock, J. Garvin, S. Sakimoto, R. Kuzmin, D. Roddy, and L. Soderblom (2000), Standardizing the nomenclature of Martian impact crater ejecta morphologies, *J. Geophys. Res.*, *105*, 26,733–26,738, doi:10.1029/2000JE001258.

Bibring, J.-P., et al. (2004), OMEGA: Observatoire pour la Minéralogie, l'Eau, les Glaces et l'Activité, in *Mars Express: The Scientific Payload*, edited by A. Wilson, *Eur. Space Agency Spec. Publ.*, *ESA SP 1240*, 37–49.

Bibring, J.-P., et al. (2005), Mars surface diversity as revealed by the OMEGA/Mars Express observations, *Science*, *307*, 1576–1581, doi:10.1126/science.1108806.

Bibring, J.-P., et al. (2006), Global mineralogical and aqueous Mars history derived from OMEGA/Mars Express data, *Science*, *312*, 400–404, doi:10.1126/science.1122659.

Bishop, J. L., and E. Murad (2005), The visible and infrared spectral properties of jarosite and alunite, *Am. Mineral.*, *90*, 1100–1107, doi:10.2138/am.2005.1700.

Bishop, J. L., J. Madejova, P. Komadel, and H. Fröschl (2002a), The influence of structural Fe, Al and Mg on the infrared OH bands in spectra of dioctahedral smectites, *Clay Miner.*, *37*, 607–616, doi:10.1180/0009855023740063.

Bishop, J. L., E. Murad, and M. D. Dyar (2002b), The influence of octahedral and tetrahedral cation substitution on the structure of smectites and serpentines as observed through infrared spectroscopy, *Clay Miner.*, *37*, 617–628, doi:10.1180/0009855023740064.

Bishop, J. L., M. D. Lane, M. D. Dyar, and A. J. Brown (2008), Reflectance and emission spectroscopy study of four groups of phyllosilicates: Smectites, kaolinite-serpentines, chlorites and micas, *Clay Miner.*, *43*, 35–54, doi:10.1180/claymin.2008.043.1.03.

Bishop, J. L., et al. (2009), Mineralogy of Juventae Chasma: Sulfates in the light-toned mounds, mafic minerals in the bedrock, and hydrated silica and hydroxylated ferric sulfate on the plateau, *J. Geophys. Res.*, *114*, E00D09, doi:10.1029/2009JE003352.

Bridges, N. T., et al. (2010), Aeolian bedforms, yardangs, and indurated surfaces in the Tharsis Montes as seen by the HiRISE camera: Evidence for dust aggregates, *Icarus*, *205*, 165–182, doi:10.1016/j.icarus.2009.05.017.

Calvin, W. M., and T. V. V. King (1997), Spectral characteristics of iron-bearing phyllosilicates: Comparison to Orgueil (CI1), Murchison and Murray (CM2), *Meteorit. Planet. Sci.*, *32*, 693–701, doi:10.1111/j.1945-5100.1997.tb01554.x.

Chapman, M. G., and K. L. Tanaka (2002), Related magma-ice interactions: Possible origins of chasmata, chaos, and surface materials in Xanthe, Margaritifer, and Meridiani Terrae, Mars, *Icarus*, *155*, 324–339, doi:10.1006/icar.2001.6735.

Christensen, P. R., and S. W. Ruff (2004), Formation of the hematite-bearing unit in Meridiani Planum: Evidence for deposition in standing water, *J. Geophys. Res.*, *109*, E08003, doi:10.1029/2003JE002233.

Christensen, P. R., et al. (2000a), Detection of crystalline hematite mineralization on Mars by the Thermal Emission Spectrometer: Evidence for near-surface water, *J. Geophys. Res.*, *105*, 9623–9642, doi:10.1029/1999JE001093.

Christensen, P. R., J. L. Bandfield, D. E. Smith, V. E. Hamilton, and R. N. Clark (2000b), Identification of a basaltic component on the Martian surface from Thermal Emission Spectrometer data, *J. Geophys. Res.*, *105*, 9609–9621, doi:10.1029/1999JE001127.

Christensen, P. R., et al. (2001a), Mars Global Surveyor Thermal Emission Spectrometer experiment: Investigation description and surface science results, *J. Geophys. Res.*, *106*, 23,823–23,871, doi:10.1029/2000JE001370.

Christensen, P., R. Morris, M. Lane, J. Bandfield, and M. Malin (2001b), Global mapping of Martian hematite mineral deposits: Remnants of water-driven processes on early Mars, *J. Geophys. Res.*, *106*, 23,873–23,885, doi:10.1029/2000JE001415.

Christensen, P. R., et al. (2004), The Thermal Emission Imaging System (THEMIS) for the Mars 2001 Odyssey Mission, *Space Sci. Rev.*, *110*, 85–130, doi:10.1023/B:SPAC.0000021008.16305.94.

Clark, B. C., et al. (2005), Chemistry and mineralogy of outcrops at Meridiani Planum, *Earth Planet. Sci. Lett.*, *240*, 73–94.

Clark, R. N., T. V. V. King, M. Klejwa, and G. A. Swayze (1990), High-resolution reflectance spectroscopy of minerals, *J. Geophys. Res.*, *95*, 12,653–12,680, doi:10.1029/JB095iB08p12653.

Clark, R. N., G. A. Swayze, R. Wise, K. E. Livo, T. M. Hoefen, R. F. Kokaly, and S. J. Sutley (2007), USGS digital spectral library, *U.S. Geol. Surv. Data Ser.*, *231*.

Cloutis, E. A., et al. (2006), Detection and discrimination of sulfate minerals using reflectance spectroscopy, *Icarus*, *184*, 121–157, doi:10.1016/j.icarus.2006.04.003.

Cloutis, E. A., M. A. Craig, J. F. Mustard, R. V. Kruzelecky, W. R. Jamroz, A. Scott, D. L. Bish, F. Poulet, J.-P. Bibring, and P. L. King (2007), Stability of hydrated minerals on Mars, *Geophys. Res. Lett.*, *34*, L20202, doi:10.1029/2007GL031267.

Cooper, C. D., and J. F. Mustard (1999), Effects of very fine particle size on reflectance spectra of smectite and palagonite soil, *Icarus*, *142*, 557–570, doi:10.1006/icar.1999.6221.

Craddock, R. A., and A. D. Howard (2002), The case for rainfall on a warm, wet early Mars, *J. Geophys. Res.*, *107*(E11), 5111, doi:10.1029/2001JE001505.

CRISM Science Team (2006), Mars Reconnaissance Orbiter CRISM Spectral Library, MRO-M-CRISM-5-SPECLIB-V1.0, *NASA Planet. Data Syst.*, Greenbelt, Md.

Crowley, J. K., D. E. Williams, J. M. Hammarstrom, N. Piatak, I.-M. Chou, and J. C. Mars (2003), Spectral reflectance properties (0.4–2.5 μm) of secondary Fe-oxide, Fe-hydroxide, and Fe-sulphate-hydrate minerals associated with sulphide-bearing mine wastes, *Geochem. Explor. Environ. Anal.*, *3*, 219–228, doi:10.1144/1467-7873/03-001.

Decarreau, A., S. Petit, F. Martin, F. Farges, P. Vieillart, and E. Joussein (2008), Hydrothermal synthesis, between 75 and 150°C, of high-charge, ferric nontronites, *Clays Clay Miner.*, *56*, 322–337, doi:10.1346/CCMN.2008.0560303.

Edgett, K. S. (2005), The sedimenatary rocks of Sinus Meridiani: Five key observations from data acquired by the Mars Global Surveyor and Mars Odyssey Orbiters, *Mars*, *1*, 5–58, doi:10.1555/mars.2005.0002.

Edgett, K. S., and M. C. Malin (2002), Martian sedimentary rock stratigraphy: Outcrops and interbedded craters of northwest Sinus Meridiani and southwest Arabia Terra, *Geophys. Res. Lett.*, *29*(24), 2179, doi:10.1029/2002GL016515.

Edgett, K. S., and T. J. Parker (1997), Water on early Mars: Possible subaqueous sedimentary deposit covering ancient cratered terrain in western Arabia and Sinus Meridiani, *Geophys. Res. Lett.*, *24*, 2897–2900, doi:10.1029/97GL02840.

Frost, R. L., J. T. Kloprogee, and Z. Ding (2002), Near-infrared spectroscopic study of nontronites and ferruginous smectite, *Geochim. Cosmochim. Acta*, *58*, 1657–1668.

Garvin, J. B., and J. J. Frawley (1998), Gemmetric properties of Martian impact craters: Preliminary results from the Mars Orbiter Laser Altimeter, *J. Geophys. Res.*, *25*, 4405–4408.

Gendrin, A., et al. (2005), Sulfates in Martian layered terrains: The OMEGA/Mars Express view, *Science*, *307*, 1587–1591, doi:10.1126/science.1109087.

Glotch, T. D., and P. R. Christensen (2005), Geologic and mineralogic mapping of Aram Chaos: Evidence for a water-rich history, *J. Geophys. Res.*, *110*, E09006, doi:10.1029/2004JE002389.

Golden, D. C., D. W. Ming, R. V. Morris, and T. G. Graff (2008), Hydrothermal synthesis of hematite spherules and jarosite: Implications for diagenesis and hematite spherule formation in sulfate outcrops at Meridiani Planum, Mars, *Am. Mineral.*, *93*, 1201–1214, doi:10.2138/am.2008.2737.

Griffes, J. L., R. E. Arvidson, F. Poulet, and A. Gendrin (2007), Geologic and spectral mapping of etched terrain deposits in northern Meridiani Planum, *J. Geophys. Res.*, *112*, E08S09, doi:10.1029/2006JE002811.

Grotzinger, J. P., et al. (2005), Stratigraphy and sedimentology of a dry to wet eolian depositional system, Burns formation, Meridiani Planum, Mars, *Earth Planet. Sci. Lett.*, *240*, 11–72, doi:10.1016/j.epsl.2005.09.039.

Hawthorne, F. C., S. V. Krivovichev, and P. C. Burns (2000), The crystal chemistry of sulfate minerals, in *Sulfate Minerals: Crystallography, Geochemistry, and Environmental Significance*, *Rev. Mineral. Geochem*, edited by C. N. Alpers et al., pp. 1–112, Mineral. Soc. of Am., Washington, D. C.

Hovorka, S. D., R. M. Holt, and D. W. Powers (2007), Depth indicators in Permian basin evaporites, in *Evaporites Through Space and Time*, edited by B. C. Schreiber et al., pp. 335–364, Geol. Soc., Bath, U. K.

Hunt, G. R., and R. P. Ashley (1979), Spectra of altered rocks in the visible and near-infrared, *Econ. Geol.*, *74*, 1613–1629, doi:10.2113/gsecongeo.74.7.1613.

Hynek, B. M. (2004), Implications for hydrologic processes on Mars from extensive bedrock outcrop throughout Terra Meridiani, *Nature*, *431*, 156–159, doi:10.1038/nature02902.

Hynek, B. M., and R. J. Phillips (2001), Evidence for extensive denudation of the Martian highlands, *Geology*, *29*(5), 407–410, doi:10.1130/0091-7613(2001)029<0407:EFEDOT>2.0.CO;2.

Hynek, B. M., and R. J. Phillips (2008), The stratigraphy of Meridiani Planum, Mars, and implications for the layered deposits' origin, *Earth Planet. Sci. Lett.*, *274*, 214–220, doi:10.1016/j.epsl.2008.07.025.

Hynek, B. M., R. E. Arvidson, and R. J. Phillips (2002), Geologic setting and origin of Terra Meridiani hematite deposit on Mars, *J. Geophys. Res.*, *107*(E10), 5088, doi:10.1029/2002JE001891.

King, T. V. V., and R. N. Clark (1989), Spectral characteristics of chlorites and Mg-serpentines using high-resolution reflectance spectroscopy, *J. Geophys. Res.*, *94*, 13,997–14,008, doi:10.1029/JB094iB10p13997.

Klingelhöfer, G., et al. (2004), Jarosite and hematite at Meridiani Planum from Opportunity's Mössbauer Spectrometer, *Science*, *306*, 1740–1745, doi:10.1126/science.1104653.

Knauth, L. P., D. M. Burt, and K. H. Wohletz (2005), Impact origin of sediments at the Opportunity landing site on Mars, *Nature*, *438*, 1123–1128, doi:10.1038/nature04383.

Knoll, A. H., et al. (2008), Veneers, rinds, and fracture fills: Relatively late alteration of sedimentary rocks at Meridiani Planum, Mars, *J. Geophys. Res.*, *113*, E06S16, doi:10.1029/2007JE002949.

Lane, M. D., P. R. Christensen, and W. K. Hartmann (2003), Utilization of the THEMIS visible and infrared imaging data for crater population studies of the Meridiani Planum landing site, *Geophys. Res. Lett.*, *30*(14), 1770, doi:10.1029/2003GL017183.

Langevin, Y., F. Poulet, J.-P. Bibring, and B. Gondet (2005), Sulfates in the northern polar region of Mars detected by OMEGA/Mars Express, *Science*, *307*, 1584–1586, doi:10.1126/science.1109091.

Lichtenberg, K. A., et al. (2010), Stratigraphy of hydrated sulfates in the sedimentary deposits of Aram Chaos, Mars, *J. Geophys. Res.*, *115*, E00D17, doi:10.1029/2009JE003353.

Malin, M. C., and K. S. Edgett (2000), Sedimentary rocks of early Mars, *Science*, *290*, 1927–1937, doi:10.1126/science.290.5498.1927.

Malin, M. C., G. E. Danielson, A. P. Ingersoll, H. Masursky, J. Veverka, M. A. Ravine, and T. A. Soulanille (1992), Mars observer camera, *J. Geophys. Res.*, *97*, 7699–7718, doi:10.1029/92JE00340.

Malin, M. C., et al. (2007), Context Camera Investigation on board the Mars Reconnaissance Orbiter, *J. Geophys. Res.*, *112*, E05S04, doi:10.1029/2006JE002808.

Mangold, N., A. Gendrin, B. Gondet, S. LeMouelic, C. Quantin, V. Ansan, J.-P. Bibring, Y. Langevin, P. Masson, and G. Neukum (2008), Spectral and geological study of the sulfate-rich region of west Candor Chasma, Mars, *Icarus*, *194*, 519–543, doi:10.1016/j.icarus.2007.10.021.

McCollom, T. M., and B. M. Hynek (2005), A volcanic environment for bedrock diagenesis at Meridiani Planum on Mars, *Nature*, *438*, 1129–1131, doi:10.1038/nature04390.

McEwen, A. S., et al. (2007), Mars Reconnaissance Orbiter's High Resolution Imaging Science Experiment (HiRISE), *J. Geophys. Res.*, *112*, E05S02, doi:10.1029/2005JE002605.

McGetchin, T. R., M. Settle, and J. W. Head (1973), Radial thickness of variation in impact crater ejecta: Implications for lunar basin deposits, *Earth Planet. Sci. Lett.*, *20*, 226–236, doi:10.1016/0012-821X(73)90162-3.

McLennan, S. M., et al. (2005), Provenance and diagenesis of the evaporite-bearing Burns formation, Meridiani Planum, Mars, *Earth Planet. Sci. Lett.*, *240*, 95–121, doi:10.1016/j.epsl.2005.09.041.

Mellon, M. T., B. M. Jakosky, H. H. Kieffer, and P. R. Christensen (2000), High-resolution thermal inertia mapping from the Mars Global Surveyor Thermal Emission Spectrometer, *Icarus*, *148*, 437–455, doi:10.1006/icar.2000.6503.

Milliken, R. E., and J. F. Mustard (2005), Quantifying absolute water content of minerals using near-infrared reflectance spectroscopy, *J. Geophys. Res.*, *110*, E12001, doi:10.1029/2005JE002534.

Morris, R. V., et al. (2006), Mössbauer mineralogy of rock, soil, and dust at Meridiani Planum, Mars: Opportunity's journey across sulfate-rich outcrops, basaltic sand and dust, and hematite lag deposits, *J. Geophys. Res.*, *111*, E12S15, doi:10.1029/2006JE002791.

Morris, R. V., D. C. Golden, D. W. Ming, T. G. Graff, R. E. Arvidson, S. M. Wiseman, K. A. Lichtenberg, and S. Cull (2009), Visible and near-IR reflectance spectra for smectite, sulfate, and perchlorate under dry conditions for interpretation of Martian surface mineralogy, *Lunar Planet. Sci.*, XXXX, Abstract 2317.

Murchie, S. L., et al. (2007), Compact Reconnaissance Imaging Spectrometer for Mars (CRISM) on Mars Reconnaissance Orbiter (MRO), *J. Geophys. Res.*, *112*, E05S03, doi:10.1029/2006JE002682.

Murchie, S. L., et al. (2009a), Compact Reconnaissance Imaging Spectrometer for Mars investigation and data set from the Mars Reconnaissance Orbiter's primary science phase, *J. Geophys. Res.*, *114*, E00D07, doi:10.1029/2009JE003344.

Murchie, S. L., et al. (2009b), Evidence for the origin of layered deposits in Candor Chasma, Mars, from mineral composition and hydrologic modeling, *J. Geophys. Res.*, *114*, E00D05, doi:10.1029/2009JE003343.

Mustard, J., et al. (2008), Hydrated silicate minerals on mars observed by the CRISM instrument on MRO, *Nature*, *454*, 305–309, doi:10.1038/nature07097.

Newsom, H. E., C. A. Barber, T. M. Hare, T. Schelble, V. A. Sutherland, and W. C. Feldman (2003), Paleolakes and impact basins in southern Arabia Terra, including Meridiani Planum: Implications for the formation of hematite deposits on Mars, *J. Geophys. Res.*, *108*(E12), 8075, doi:10.1029/2002JE001993.

Newsom, H. E., et al. (2010), Inverted channel deposits on the floor of Miyamoto crater, Mars, *Icarus*, *205*, 64–72.

Niles, P. B., and J. Michalski (2009), Meridiani Planum sediments on Mars formed through weathering in massive ice deposits, *Nat. Geosci.*, *2*, 215–220, doi:10.1038/ngeo438.

Noe Dobrea, E. Z., F. Poulet, and M. C. Malin (2008), Correlations between hematite and sulfates in the chaotic terrain east of Valles Marineris, *Icarus*, *193*, 516–534, doi:10.1016/j.icarus.2007.06.029.

Pelkey, S. M., et al. (2007), CRISM multispectral summary products: Parameterizing mineral diversity on Mars from reflectance, *J. Geophys. Res.*, *112*, E08S14, doi:10.1029/2006JE002831.

Phillips, R. J., et al. (2001), Ancient geodynamics and global-scale hydrology of Mars, *Science*, *291*, 2587–2591, doi:10.1126/science.1058701.

Poulet, F., J.-P. Bibring, J. F. Mustard, A. Gendrin, N. Mangold, Y. Langevin, R. E. Arvidson, B. Gondet, and C. Gomez (2005), Phyllosilicates on Mars and implications for early Martian climage change, *Nature*, *438*, 623–627, doi:10.1038/nature04274.

Poulet, F., R. E. Arvidson, C. Gomez, R. V. Morris, J.-P. Bibring, Y. Langevin, B. Gondet, and J. Griffes (2008), Mineralogy of Terra Meridiani and western Arabia Terra from OMEGA/MEx and implications for their formation, *Icarus*, *195*, 106–130, doi:10.1016/j.icarus.2007.11.031.

Putzig, N. E., and M. T. Mellon (2007), Apparent thermal inertia and the surface heterogeneity of Mars, *Icarus*, *191*, 68–94, doi:10.1016/j.icarus.2007.05.013.

Rieder, R., et al. (2004), Chemistry of rocks and soils at Meridiani Planum from Alpha Particle X-ray Spectrometer, *Science*, *306*, 1746–1749, doi:10.1126/science.1104358.

Rotto, S., and K. L. Tanaka (1995), Geologic/geomorphic map of the Chryse Planitia region of Mars, *U.S. Geol. Surv. Misc. Invest. Map*, *I-244*.

Salvatore, M. R., M. J. Wilkinson, C. C. Allen, and D. Z. Oehler (2008), Terresterial megafans as an analog for ridged unit of SW Arabia Terra, Mars: Current observations and future analysis, *Lunar Planet. Sci.*, XXXIX, Abstract 1455.

Schultz, P. H., and A. B. Lutz (1988), Polar wandering of Mars, *Icarus*, *73*, 91–141, doi:10.1016/0019-1035(88)90087-5.

Scott, D. H., and K. L. Tanaka (1986), Geologic map of the western equatorial region of Mars, *U.S. Geol. Surv. Misc. Invest. Map*, *I-1802-A*.

Smith, D. E., et al. (2001), Mars Orbiter Laser Altimeter: Experiment summary after the first year of global mapping of Mars, *J. Geophys. Res.*, *106*, 23,689–23,722, doi:10.1029/2000JE001364.

Squyres, S. W., et al. (2004a), The Opportunity Rover's Athena science investigation at Meridiani Planum, Mars, *Science*, *306*, 1698–1703, doi:10.1126/science.1106171.

Squyres, S. W., et al. (2004b), In situ evidence for an ancient aqueous environment at Meridiani Planum, Mars, *Science*, *306*, 1709–1714, doi:10.1126/science.1104559.

Squyres, S. W., et al. (2006), Two years at Meridiani Planum: Results from the Opportunity Rover, *Science*, *313*, 1403–1407, doi:10.1126/science.1130890.

Stamnes, K., S. Tsay, W. Wiscombe, and K. Jayaweera (1988), Numerically stable algorithm for discrete-ordinate-method radiative transfer in multiple scattering and emitting layered media, *Appl. Opt.*, *27*, 2502–2509, doi:10.1364/AO.27.002502.

Stoffregen, R. E., C. N. Alpers, and J. L. Jambor (2000), Alunite-jarosite crystallography, thermodynamics, and geochemistry, in *Sulfate Minerals: Crystallography, Geochemistry, and Environmental Significance*, *Rev. Mineral. Geochem*, edited by C. N. Alpers et al., pp. 453–480, Mineral. Soc. of Am., Washington, D. C.

Sullivan, R., et al. (2005), Aeolian processes at the Mars Exploration Rover Meridiani Planum landing site, *Nature*, *436*, 58–61, doi:10.1038/nature03641.

Swayze, G. A., R. N. Clark, S. J. Sutley, C. A. Gent, B. W. Rockwell, D. L. Blane, J. L. Post, and B. P. Farm (2002), Mineral mapping Mauna Kea and Mauna Loa shield volcanos on Hawaii using AVIRIS data and the USGS Tetracorder spectral identification system: Lessons applicable to the search for relict Martian hydrothermal systems, in *Proceedings of the 11th JPL Airborne Earth Science Workshop*, edited by R. O. Green, *JPL Publ. 03-4*, 373–387.

Wiseman, S. M. (2009), Retrieval of atmospherically corrected hyperspectral CRISM surface reflectance spectra using DISORT radiative transfer modeling: Comparison to the empirical 'volcano scan' correction method, in Spectral and stratigraphic mapping of hydrated sulfate and phyllosilicate-bearing deposits: Implications for the aqueious history of Sinus Meridiani, Mars, Ph.D. dissertation, pp. 5–50, Washington Univ. in St. Louis, St. Louis, Mo.

Wiseman, S. M., et al. (2007), Initial analysis of CRISM data over Meridiani Planum, *Lunar Planet. Sci.*, *XXXVIII*, Abstract 1945.

Wiseman, S. M., et al. (2008), Phyllosilicate and sulfate-hematite deposits within Miyamoto crater in southern Sinus Meridiani, Mars, *Geophys. Res. Lett.*, *35*, L19204, doi:10.1029/2008GL035363.

Wolff, M. J., M. D. Smith, R. T. Clancy, R. E. Arvidson, M. Kahre, F. P. Seelos IV, S. Murchie, and H. Savijärvi (2009), Wavelength dependence of dust aerosol single scattering albedo as observed by CRISM, *J. Geophys. Res.*, *114*, E00D04, doi:10.1029/2009JE003350.

J. C. Andrews-Hanna, Department of Geophysics, Colorado School of Mines, Golden, CO 80401, USA.

R. E. Arvidson and S. M. Wiseman, McDonnell Center for the Space Sciences, Department of Earth and Planetary Sciences, Washington University in Saint Louis, Saint Louis, MO 63130, USA.

J. L. Bishop, SETI Institute, Mountain View, CA 94043, USA.

D. Des Marais, NASA Ames Research Center, Moffett Field, CA 94035, USA.

J. L. Griffes, Division of Geological and Planetary Sciences, California Institute of Technology, Pasadena, CA 91106, USA.

R. V. Morris, NASA Johnson Space Center, Houston, TX 77058, USA.

S. L. Murchie and F. P. Seelos, Johns Hopkins University Applied Physics Laboratory, Laurel, MD 20723, USA.

F. Poulet, Institut d' Astrophysique Spatiale, Université Paris-Sud, F-91405 Orsay, France.